

**Electronic Supplementary Information (ESI) for Energy &
Environmental Science**

A pH-universal ORR catalyst with iron single-atom sites derived from double-layer MOF: superior flexible quasi-solid-state rechargeable Zn-air batteries

Meiqi Zhao,^a Haoran Liu,^a Hongwei Zhang,^a Wen Chen,^a Hanqin Sun,^a Zhenhua Wang,^a Biao Zhang,^a Lin Song,^a Yong Yang,^d Chao Ma,^e Yunhu Han,^{*a,b,c} and Wei Huang^{*a}

^aFrontiers Science Center for Flexible Electronics, Xi'an Institute of Flexible Electronics (IFE) and Xi'an Institute of Biomedical Materials & Engineering, Northwestern Polytechnical University, Xi'an 710072, China.

^bState Key Laboratory of Structural Chemistry, Fujian Institute of Research on the Structure of Matter, Chinese Academy of Sciences, Fuzhou, Fujian 350002, China.

^cKey Laboratory for Organic Electronics and Information Displays & Institute of Advanced Materials (IAM), Nanjing University of Posts and Telecommunications, 9 Wenyuan Road, Nanjing 210023, China.

^dS State Key Laboratory of Solidification Processing, Center of Advanced Lubrication and Seal Materials, Northwestern Polytechnical University, Xi'an, Shaanxi 710072, P. R. China.

^eDepartment of Chemistry, Tsinghua University, Beijing 100084, China.

Corresponding authors: iamyhhan@nwpu.edu.cn (Y. H. Han), iamwhuang@nwpu.edu.cn (W. Huang)

1. Characterizations and texts

Characterizations

Powder X-ray diffractometer (PXRD) was carried out with a Rigaku RU-200b X-ray powder diffractometer with Cu K α radiation ($\lambda = 1.5406 \text{ \AA}$), 2° min^{-1} . Scanning electron microscope (SEM) was operated by a Hitachi S4800 (30 kV) electron microscope. Transmission electron microscope (TEM) was performed on a Hitachi H-800. The as-prepared catalysts were characterized by high resolution TEM (HR-TEM) and high-angle annular dark-field energy-dispersive spectrum (HAADF-EDS, JEOL-2100F FETEM) operated at 200 kV. The Brunauer-Emmett-Teller (BET) surface area of the catalyst was measured at a relative pressure of $P/P_0 = 0.00-0.40$ by using experimental points. Raman spectra were collected on an inVia Renishaw Raman spectrometer system (HR Micro Raman spectrometer, Horiba JOBIN YVON US/ HR800 UV) using a 632.8 nm wavelength laser. Inductively coupled plasma mass spectrometer (ICP-MS) was carried out on an Optima 7300 DV. X-ray photoelectron spectrometer (XPS) was operated by a ULVAC PHI Quantera microscope machine.

XAFS measurement and analysis details

The X-ray absorption fine structure spectra was acquired at 1W1B station in Beijing Synchrotron Radiation Facility (BSRF, operated at 2.5 GeV with an average current of 250 mA, Fe k -edge). The data of Fe₁/ d -CN was collected in fluorescence mode, while the Fe foil as reference was measured in a transmission mode using ionization chamber at room temperature. The acquired EXAFS data were processed according to the standard procedures using the ATHENA module of Demeter software packages. The

k^3 -weighted EXAFS spectra were obtained by subtracting the post-edge background from the overall absorption and then normalizing with respect to the edge-jump step. Subsequently, k^3 -weighted $\chi(k)$ data of Fe K -edge were Fourier transformed to real (R) space using a hanning windows ($dk=1.0 \text{ \AA}^{-1}$) to separate the EXAFS contributions from different coordination shells. To obtain the quantitative structural parameters around central atoms, least-squares curve parameter fitting was performed using the ARTEMIS module of Demeter software packages. The following EXAFS equation was used:

$$\chi(k) = \sum_j \frac{N_j S_o^2 F_j(k)}{k R_j^2} \exp[-2 k^2 \sigma_j^2] \exp\left[-\frac{2 R_j}{\lambda(k)}\right] \sin[2k R_j + \phi_j(k)]$$

S_o^2 is the amplitude reduction factor, $F_j(k)$ is the effective curved-wave backscattering amplitude, N_j is the number of neighbors in the j^{th} atomic shell, R_j is the distance between the X-ray absorbing central atom and the atoms in the j^{th} atomic shell (backscatterer), λ is the mean free path in \AA , $\phi_j(k)$ is the phase shift (including the phase shift for each shell and the total central atom phase shift), σ_j is the Debye-Waller parameter of the j^{th} atomic shell (variation of distances around the average R_j). The functions $F_j(k)$, λ and $\phi_j(k)$ were calculated with the ab initio code FEFF9.

Electrochemical Measurements: Electrochemical performance of the catalysts were carried out on a CHI760E electrochemical station (CH Instruments, Inc., Shanghai) with a conventional three-electrode system in 0.1M KOH, 0.5M H₂SO₄ and 0.1 M PBS solutions, respectively. The working electrode is the rotating disk electrode (RDE) with a 5 mm-diameter GC disk or the rotating ring-disk electrode (RRDE) with a 5.5 mm-diameter GC disk and a Pt ring of 6.5 mm inter diameter and 8.5 mm outer diameter.

The counter electrode and reference electrode are graphite rod and Ag/AgCl (saturated KCl solution), respectively. The non-noble-metal catalyst inks were prepared by blending 10 mg of as-synthesized catalyst (*s*-CN, Fe NPs/*s*-CN and Fe₁/*d*-CN) with 985 μ l ethanol and 15 μ l Nafion solution (5 wt%) by sonication for 30 min. Then, 10 μ l of catalyst dispersion was deposited onto the GC surface, leading to the loading mass of 0.51 mg cm⁻². The 20% Pt/C ink as comparation was prepared by dispersing 5 mg of Pt/C in 1 ml solution (985 μ l ethanol and 15 μ l Nafion solution (5 wt%)) following an ultrasonic bath for 30 min. 10 μ l of Pt/C ink was then pipetted onto the GC surface, leading to the loading mass of 0.26 mg cm⁻². The cyclic voltammetry (CV) test with a scan rate of 50 mV s⁻¹ and the liner sweep voltammetry (LSV) technique with a scan rate of 10 mV s⁻¹ (400 rpm-2025 rpm) were measured in O₂-saturated 0.1M KOH (voltage range: 0.2 V to -0.6 V(vs. SCE)), 0.5 M H₂SO₄ (voltage range: 1.0 V to 0.0 V(vs. SCE)), or 0.1 M PBS solution (voltage range: 0.3 V to -0.6 V(vs. SCE)). Methanol tolerance was tested by chronoamperometric measurements at -0.1 V (0.6 V, -0.1 V) in a O₂-saturated mixed solution containing 0.1M KOH (0.5 M H₂SO₄, 0.1 M PBS solution) and injection of 5 ml methanol. All potentials in this work were converted to the reversible hydrogen electrode (RHE) by the formula:

$$E(\text{vs. RHE}) = E(\text{vs. Ag/AgCl}) + 0.059 \times PH + 0.196$$

The kinetic current density was calculated according to the Koutecky-Levich (K-L) equation:

$$\frac{1}{J} = \frac{1}{J_k} + \frac{1}{J_L} = \frac{1}{Bw^{1/2}} + \frac{1}{J_k}$$

$$B = 0.62nFC_0D_0^{\frac{2}{3}}V^{-\frac{1}{6}}$$

Where J is the measurement, J_k is the kinetic current and J_L is the limit current. Then, w is the angular velocity of the disk, n is the electron transfer number, F is the Faraday constant (96485 C mol⁻¹), C_0 is the volume concentration of O₂ (1.2 × 10⁻⁶ mol cm⁻³), D_0 is the diffusion coefficient of O₂ (1.9 × 10⁻⁵ cm² s⁻¹), and ν is the kinematic viscosity of the electrolyte (0.01 cm² s⁻¹).

Then, the transferred electron number (n) was calculated with the following equation:

$$n = 4 \times \frac{I_d}{I_d + I_r/N_c}$$

and H₂O₂ yield was calculated with the formular of

$$H_2O_2\% = 200 \frac{\frac{I_r}{N_c}}{I_d + \frac{I_r}{N_c}}\%$$

where I_d , I_r and N_c are the disk current, ring current and the collection efficiency of the ring disk electrode (0.424), respectively.

Quasi-solid-state Zinc-air battery assembly: In a typical assembly for the solid-state Zinc-air battery, a polished Zn foil (2 × 2 cm², with another 2 × 2 cm² left blank as current collector) was employed as the anode, catalysts coated on carbon cloth (2 × 2 cm², with another 2 × 2 cm² left blank as current collector) were pressed to top of gel polymer as the cathode, then two pieces of white breathable tapes were used to seal the device. As for the catalyst inks, we prepared by blending 10 mg of the Fe₁/d-CN catalyst with 985 μL ethanol and 15 μL Nafion solution (5 wt%) by sonication for 30 min. As a contrast, 5 mg of commercial precious metal catalysts (Pt/C: RuO₂ = 1: 1, molar ratio)

and 15 μ L of 5 wt% Nafion solution were dispersed in 985 μ L ethanol with sonication for 30 min. The mass loading of the catalysts was 2.50 and 1.25 mg cm⁻² of the Fe_{1/d}-CN-based battery and Pt/C+RuO₂-based battery, respectively. The gel polymer electrolyte was prepared briefly as follow: polyvinyl alcohol (4 g) powder was dissolved into 40 ml DIW at 95 °C under stirring until the solution became homogeneous and transparent. Then, 4 ml of 18 M KOH was added dropwise for another 40 min at 95 °C under stirring. After that, the solution was poured onto a mould and freezed in a freezer at -20 °C for 2 h with 0 °C for 4 h. As for the neutral electrolyte, we just replaced KOH solution with 6 ml of 11.8 M NH₄Cl and 2.6 M ZnCl₂, and extended the freezing time at -20 °C to 72 h. The gel polymer electrolytes were obtained after thawing at room temperature.

Liquid Zn-air battery assembly: Homemade simple alkaline/neutral liquid Zn-air batteries were built by using carbon paper coated with the Fe_{1/d}-CN catalyst as the air cathode, Zn foil as the anode, and 6 M KOH and 0.2 M Zn(ac)₂ as the alkaline electrolyte and 4 M NH₄Cl+2M KCl as the neutral electrolyte. The effective contact area between the catalyst and the electrolyte coated on carbon paper is 1 cm². The mass loading of the Fe_{1/d}-CN catalyst on carbon paper was about 2 mg cm⁻². In addition, Pt/C and RuO₂ were mixed at a molar ratio of 1:1 as control sample. The specific capacity could be calculated according to the following equation:

specific capacity = [discharge current (mA) × time (h)]/ weight of consumed Zn (g)
energy density = {[current (mA) × time (h)] /weight of consumed Zn (kg)} × discharge voltage (V)

2. Supplementary Figures and Tables

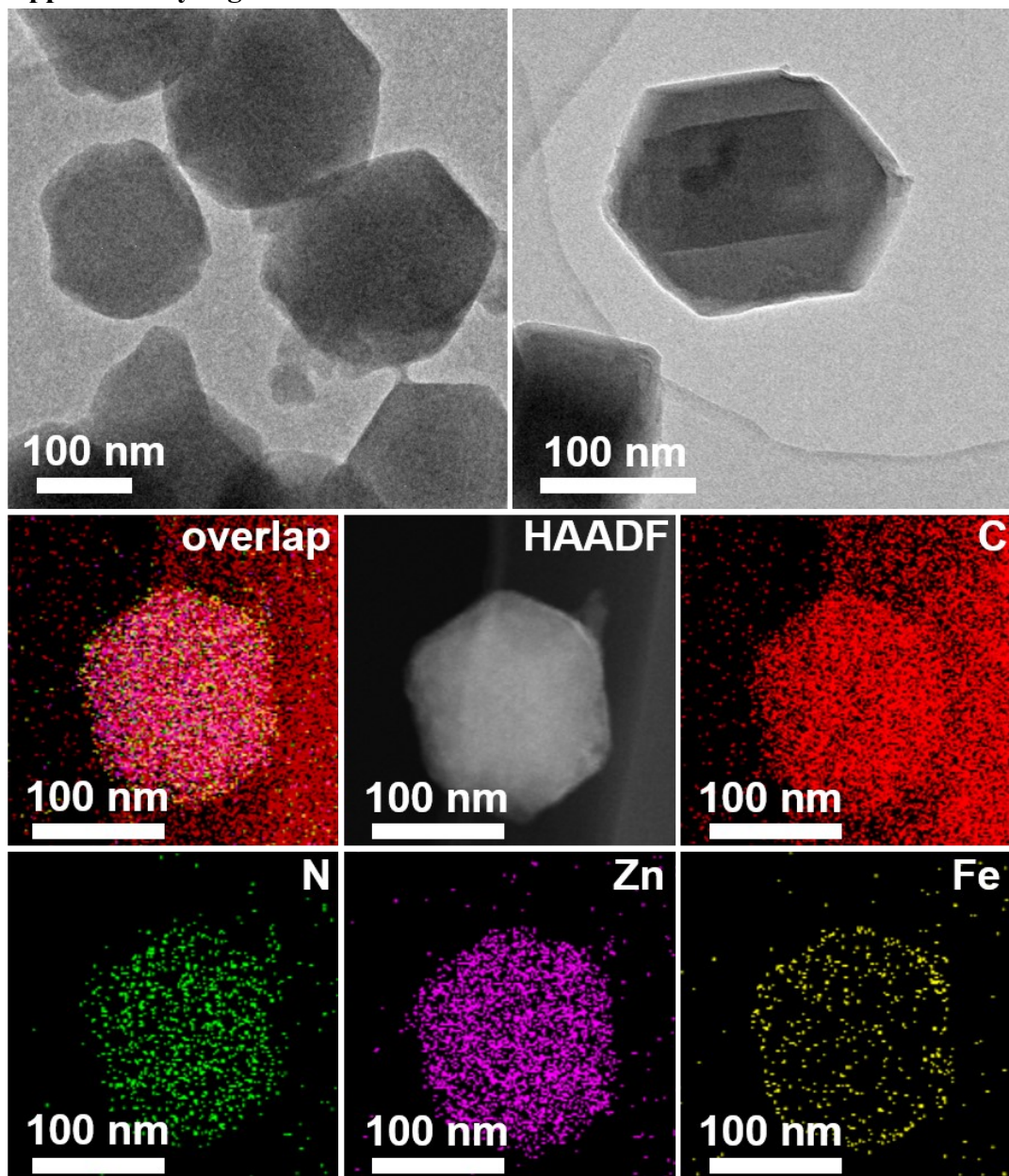


Fig. S1 HRTEM images and EDS mapping spectra of precursor Fe/ZIF-8@ZIF-8.

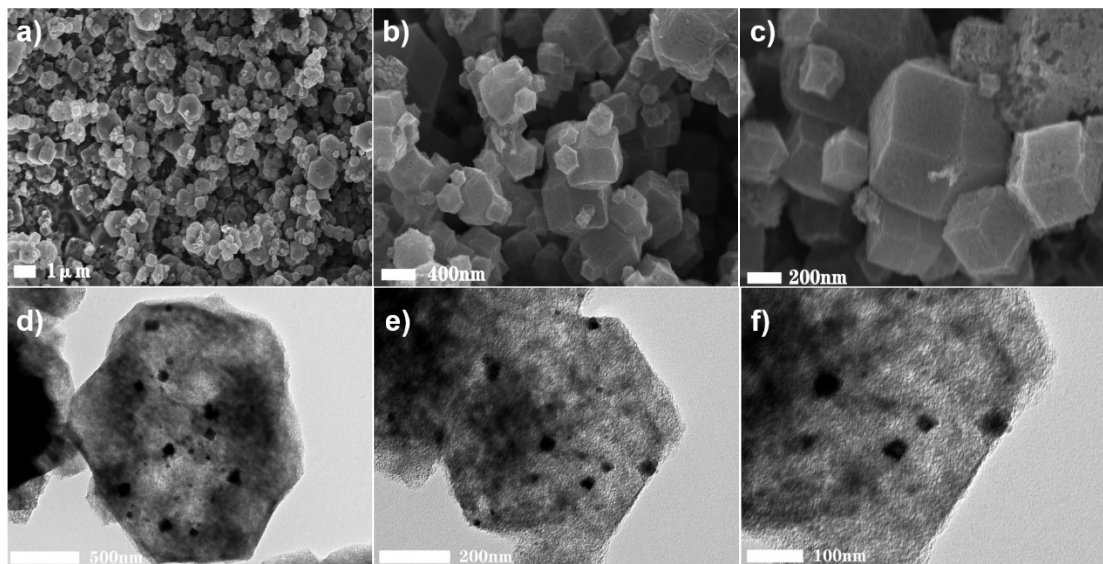


Fig. S2 (a-c) SEM images, and (d-f) TEM images of the Fe NPs/s-CN catalyst.

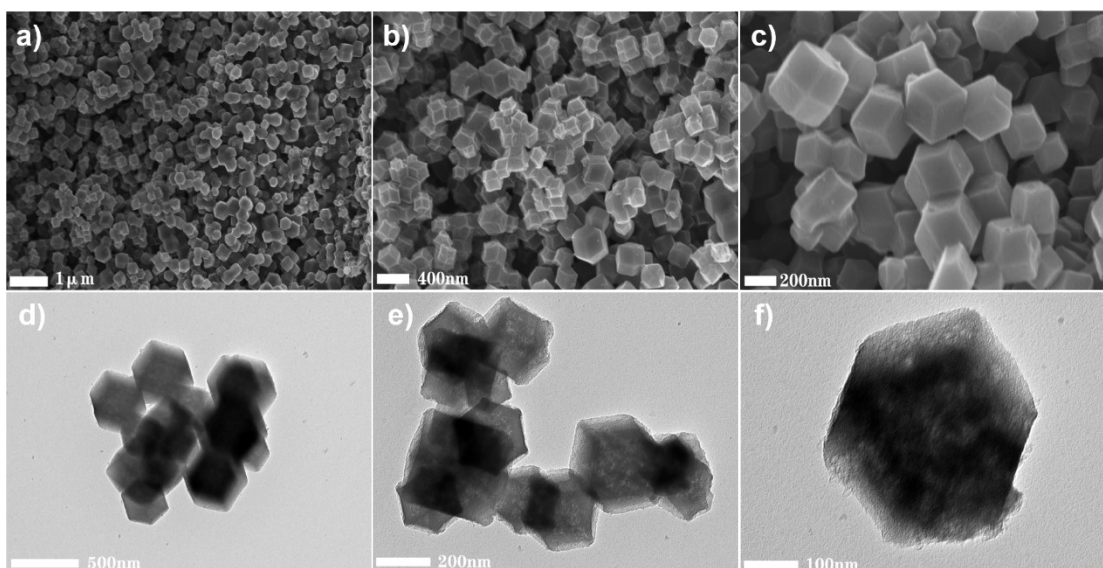


Fig. S3 (a-c) SEM images, and (d-f) TEM images of the *s*-CN catalyst.

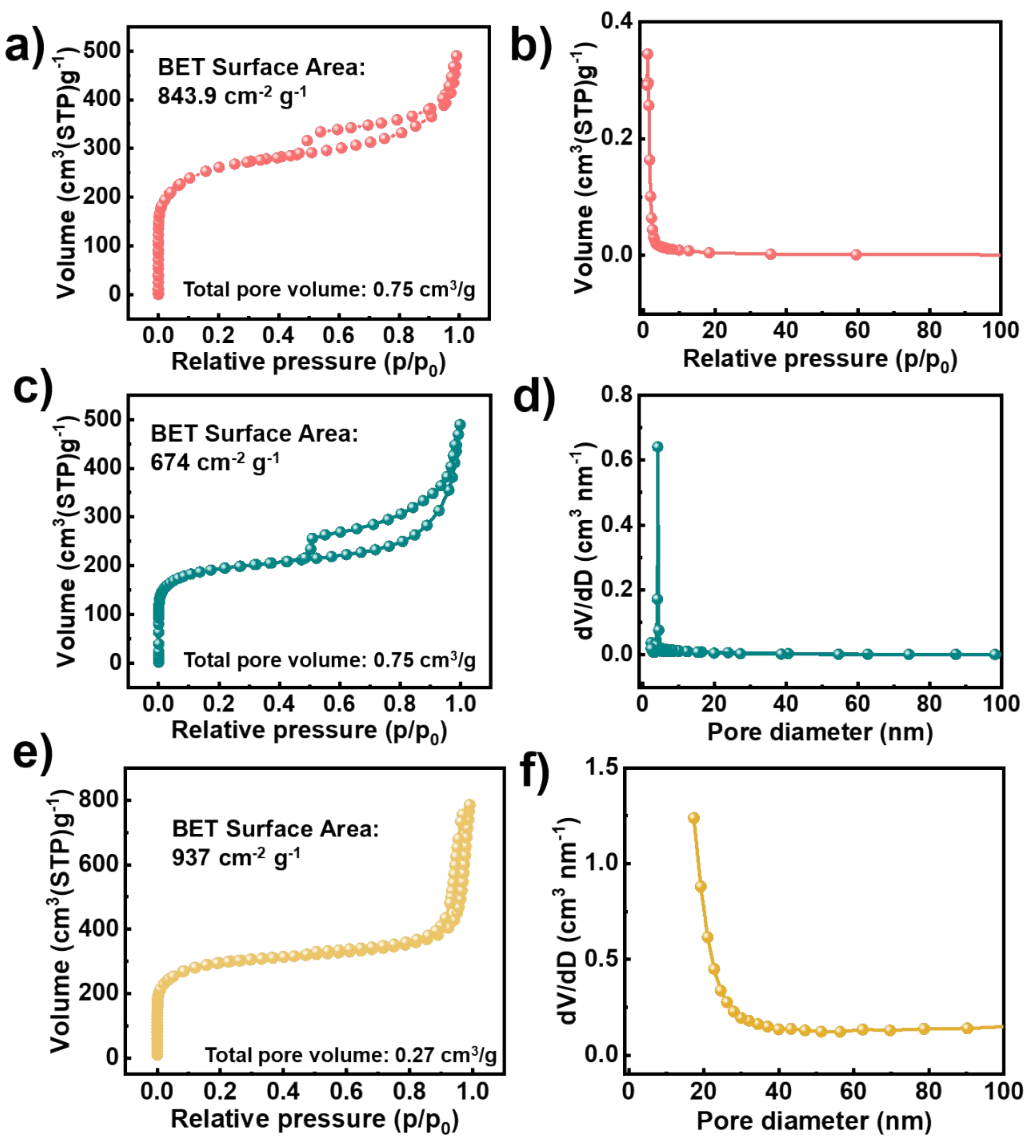


Fig. S4 N_2 adsorption desorption isotherm and pore size distributions of the $\text{Fe}_1/d\text{-CN}$ (a, b), $\text{Fe NPs}/s\text{-CN}$ (c, d), $s\text{-CN}$ (e, f) catalysts.

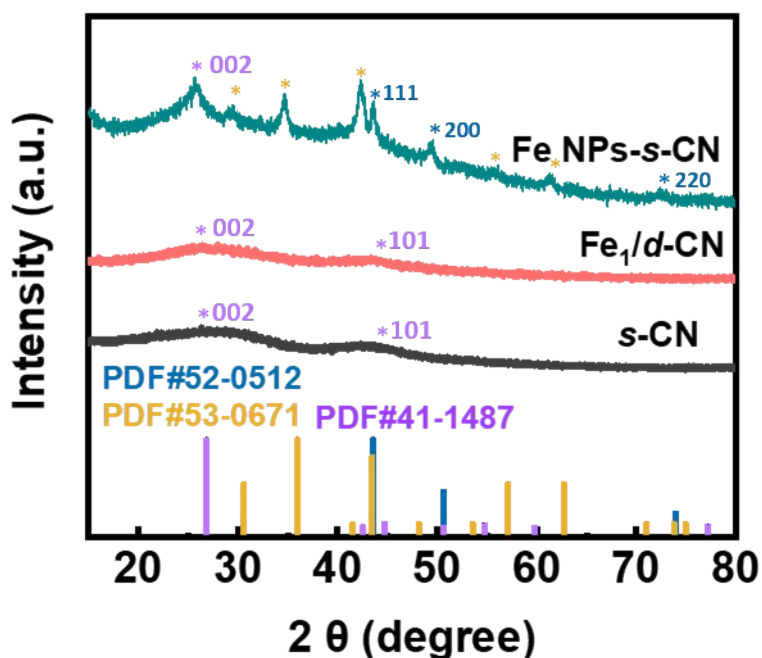


Fig. S5 PXRD patterns of the Fe₁/d-CN, Fe NPs/s-CN and s-CN catalysts.

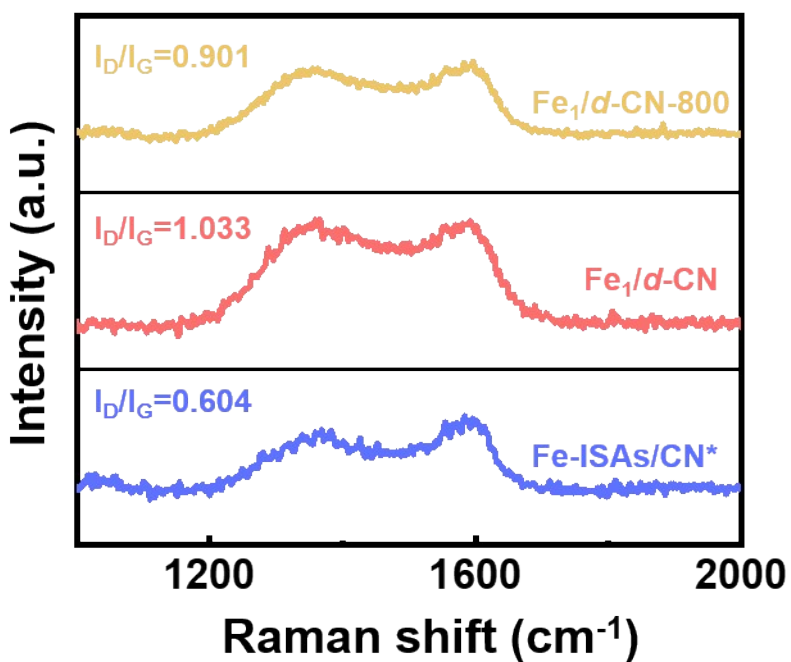


Fig. S6 Raman spectra of the Fe₁/d-CN-800, Fe₁/d-CN and Fe-ISAs/CN catalysts.* Fe-ISAs/CN is synthesized from the pyrolysis of Fe(acac)₃@ZIF-8 referred to the reported method.¹

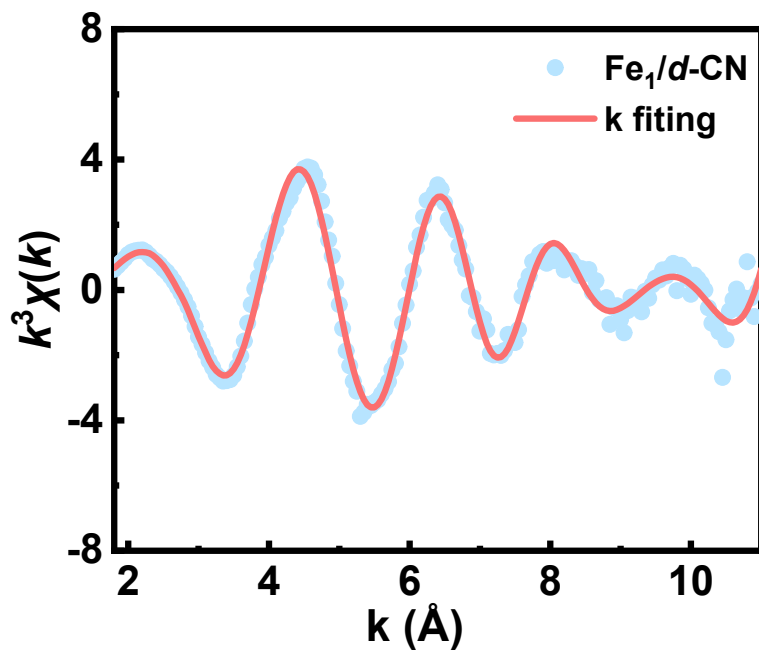


Fig. S7 FT-EXAFS fitting curves of Fe K-edge for the $\text{Fe}_1/d\text{-CN}$ catalyst at k space.

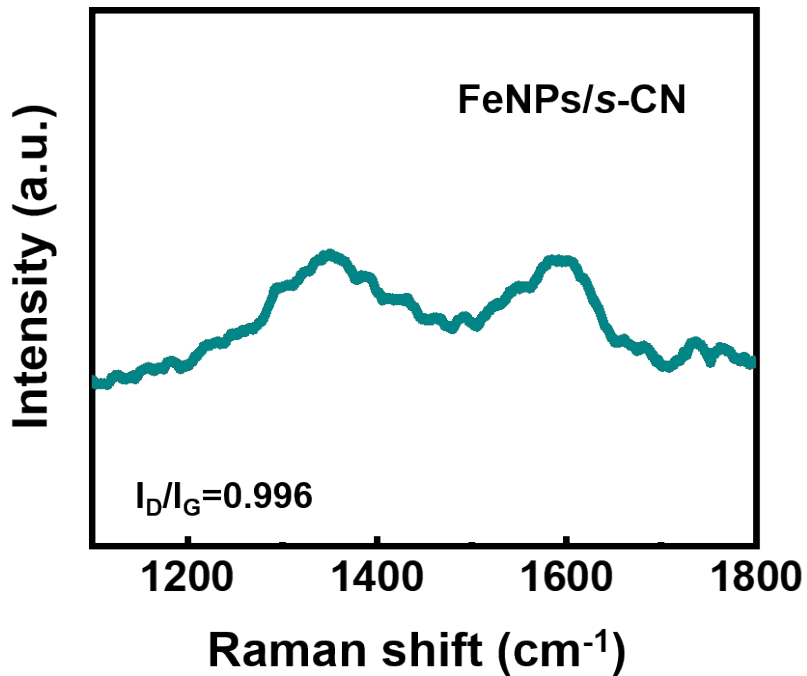


Fig. S8 Raman spectra of the FeNPs/s-CN catalyst.

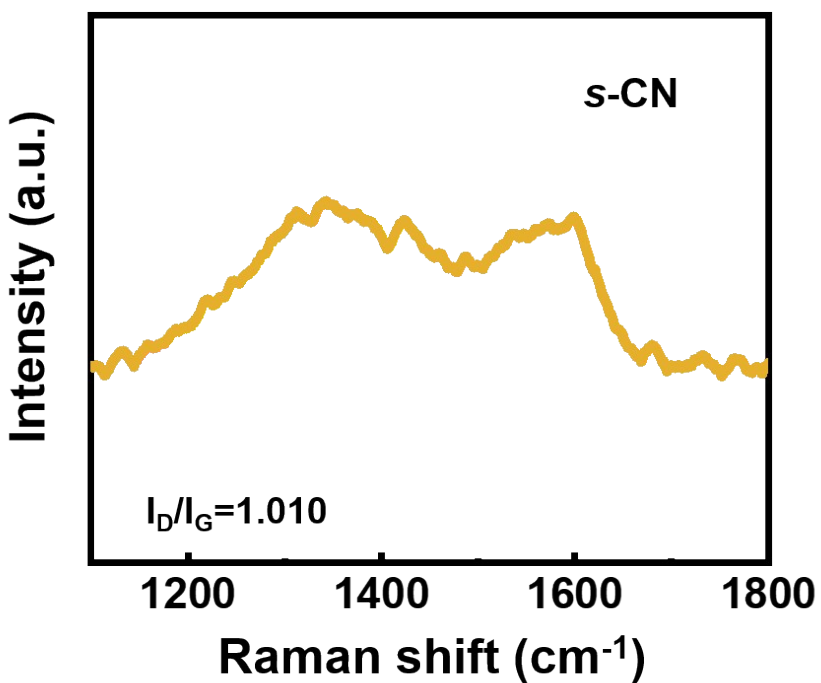


Fig. S9 Raman spectra of the *s*-CN catalyst

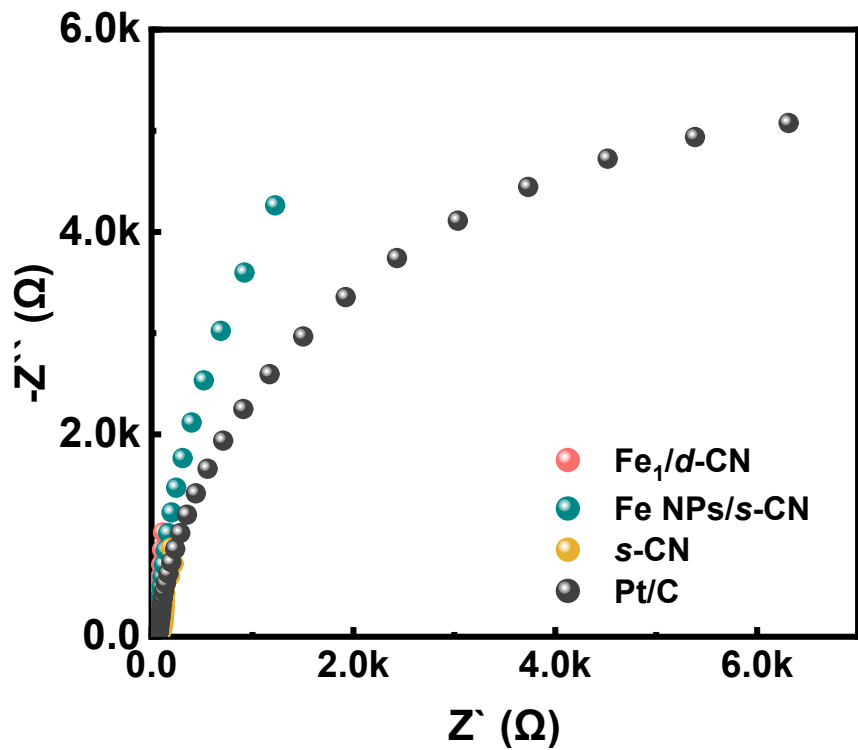


Fig. S10 Nyquist plots of the $\text{Fe}_1/d\text{-CN}$ catalyst and control samples in O_2 saturated 0.1 M KOH solution.

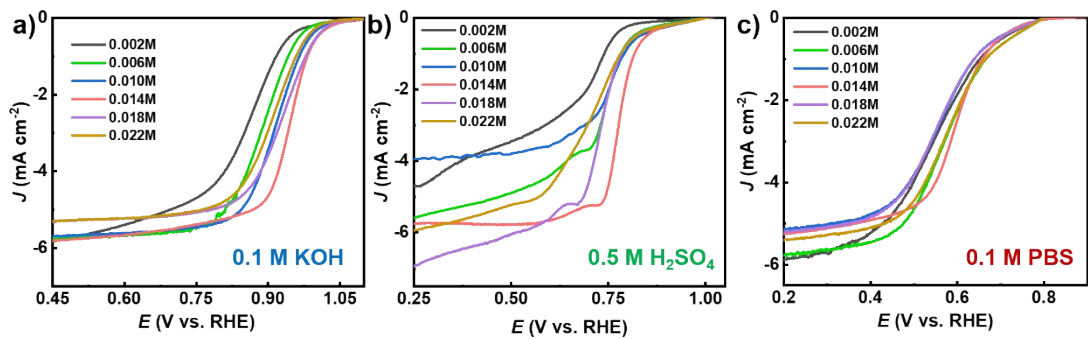


Fig. S11 LSV curves of ORR for the Fe catalysts pyrolyzed from the precursors of different Fe concentrations (Fe(acac)₃ concentration: 0.002 M, 0.006 M, 0.010 M, 0.014 M, 0.018 M and 0.022 M) at a rotating rate of 1600 rpm in O₂-saturated (a) 0.1 M KOH, (b) 0.5 M H₂SO₄ and 0.1 M PBS media.

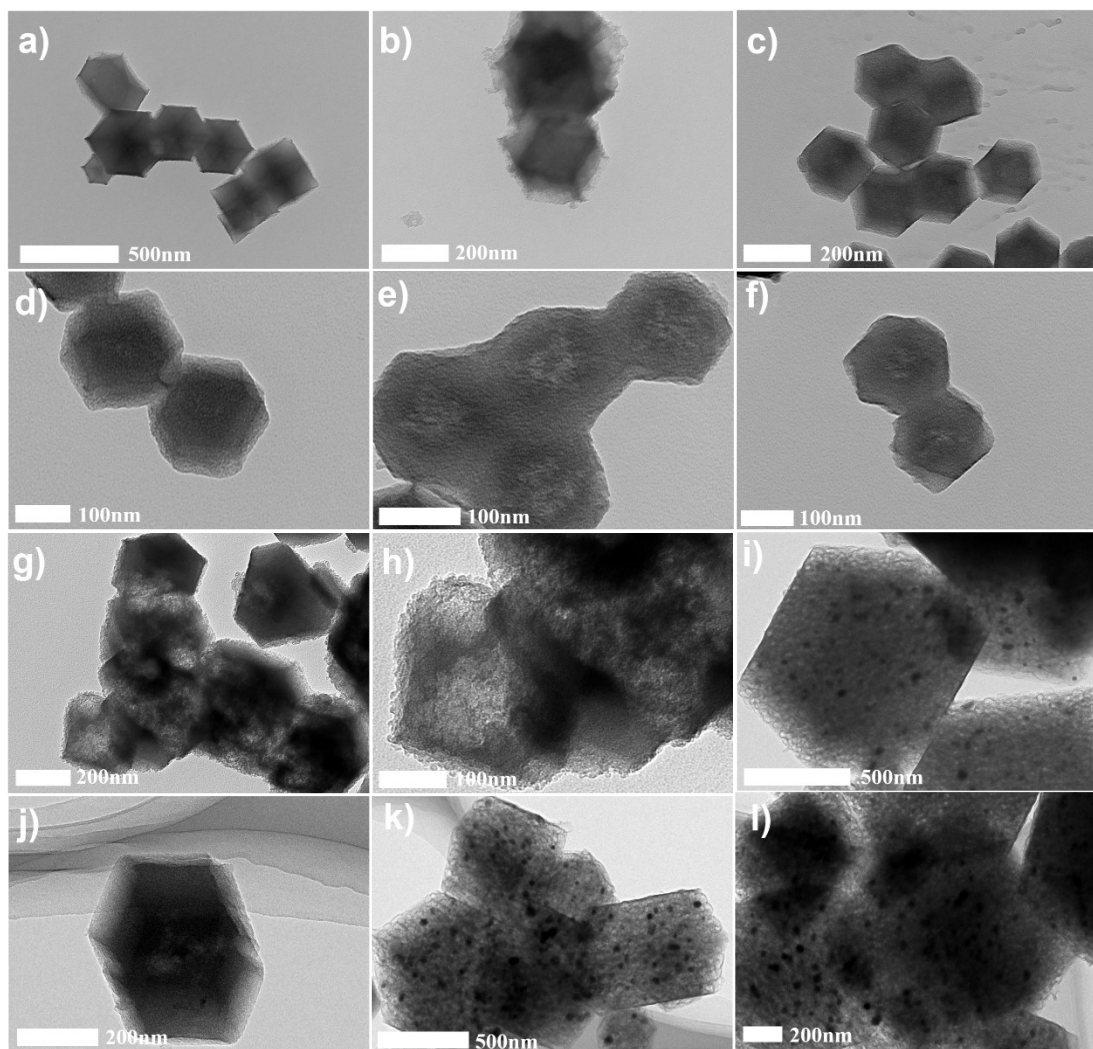


Fig. S12 TEM images of the Fe catalysts with pyrolysis of precursors of different concentration gradients ranging from 0.002 M (a,b), 0.006 M (c,d), 0.010 M (e,f), 0.014 M (g,h), 0.018 M (i,j), to 0.022 M (k,l) of $\text{Fe}(\text{acac})_3$.

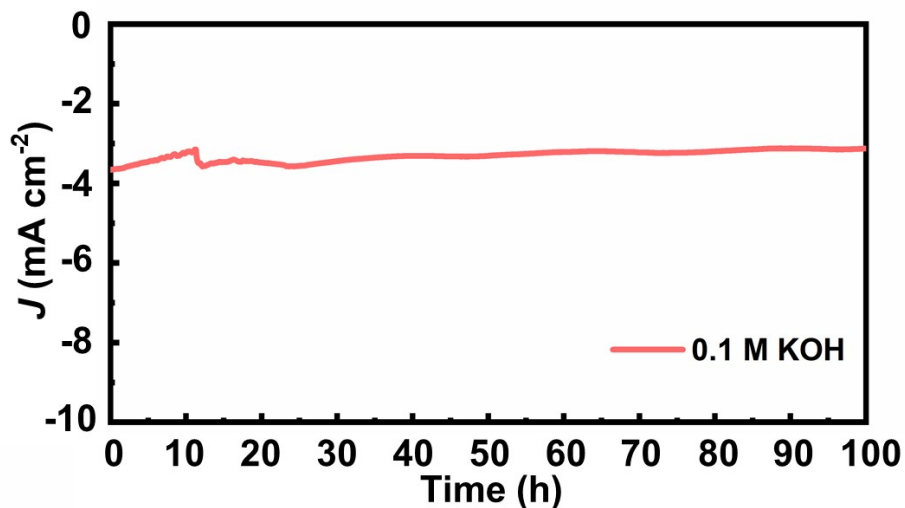


Fig. S13 I-t chronoamperometric responses of the $\text{Fe}_1/d\text{-CN}$ catalyst in the alkaline media.

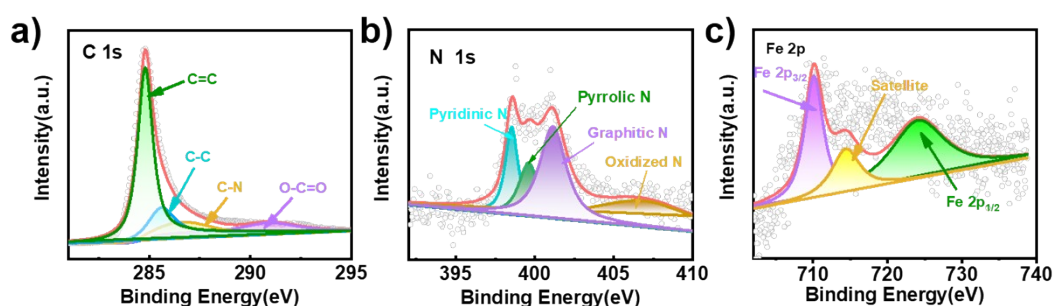


Fig. S14 High-resolution XPS spectra of (a) C 1s, (b) N 1s, and (c) Fe 2p for $\text{Fe}_1/d\text{-CN}$ catalyst after 30 k CV cycles in 0.1 M KOH solution.

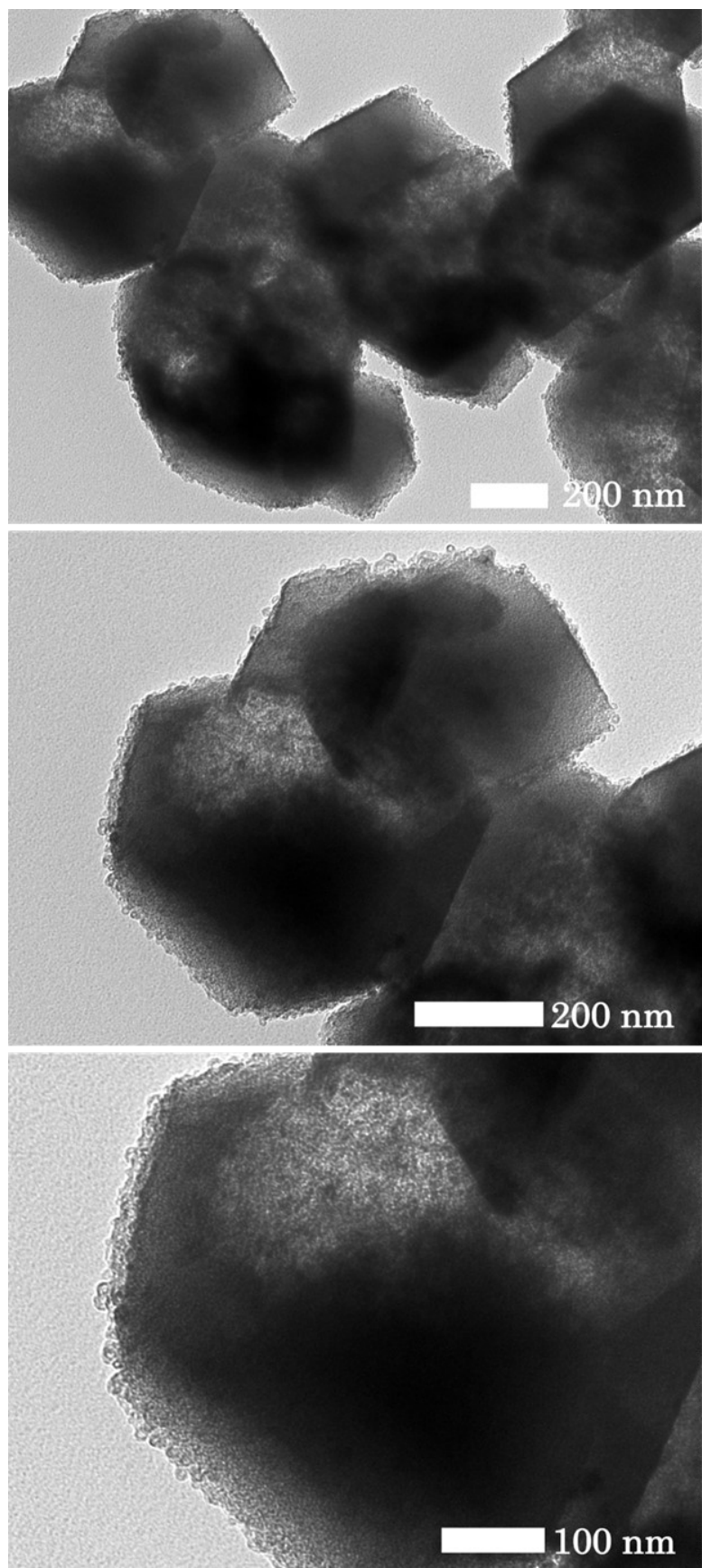


Fig. S15 TEM images of the $\text{Fe}_{1/d}\text{-CN}$ catalyst after 30 k CV cycles in 0.1 M KOH solution.

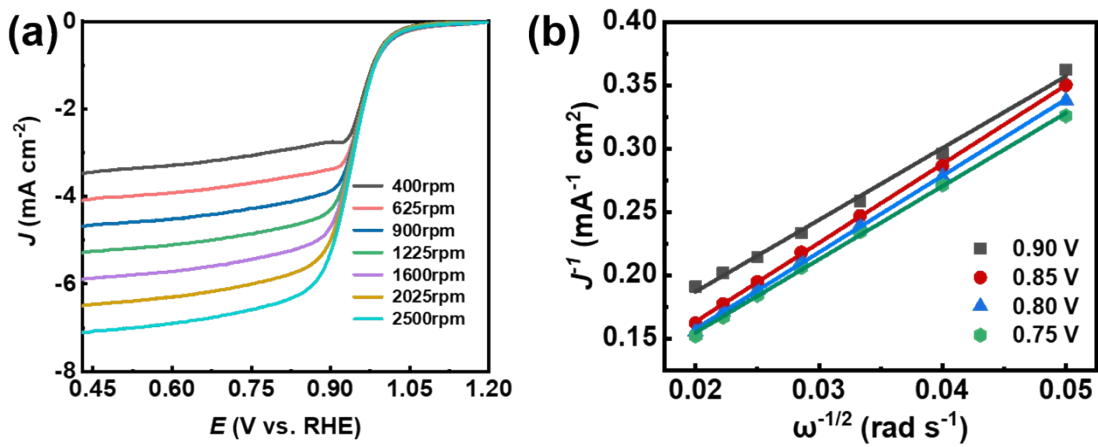


Fig. S16 (a) LSV curves at different rotating rates, and (b) Koutecky-Levich (K-L) plots of the $\text{Fe}_1/d\text{-CN}$ catalyst in O_2 saturated 0.1 M KOH solution.

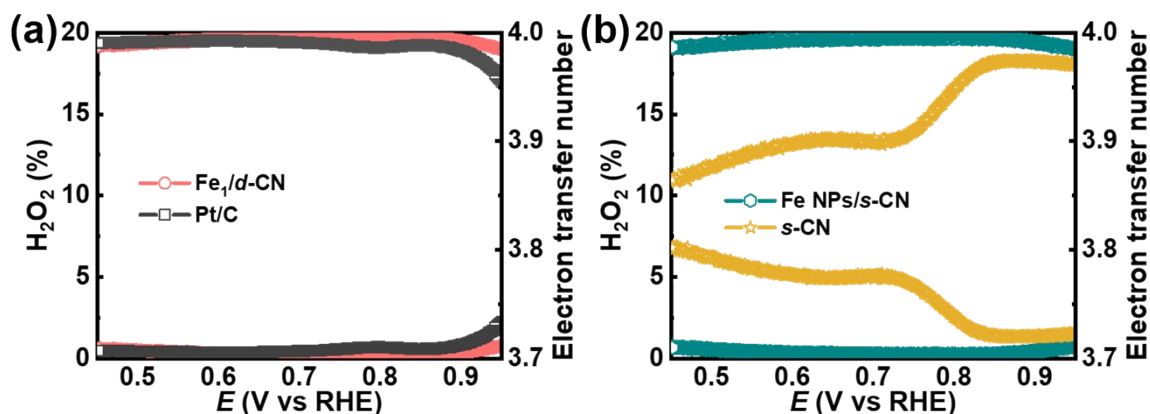


Fig. S17 Electron transfer number and peroxide yield derived from ring-disk voltammograms of the $\text{Fe}_1/d\text{-CN}$, Fe NPs/s-CN, s-CN and commercial Pt/C catalysts in O_2 saturated 0.1 M KOH solution.

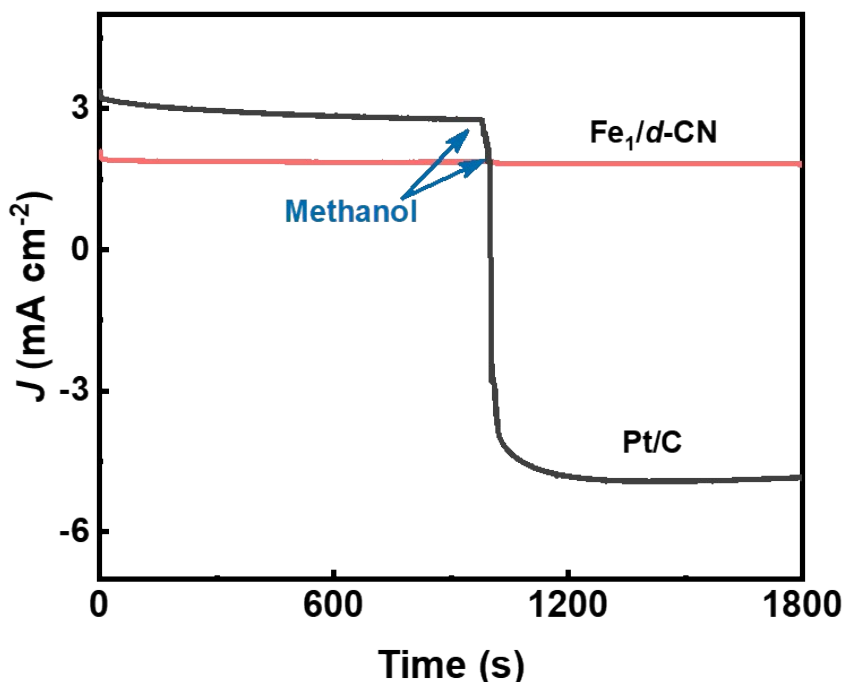


Fig. S18 Methanol tolerance of the $\text{Fe}_1/d\text{-CN}$ and commercial Pt/C catalysts in O_2 saturated 0.1 M KOH solution.

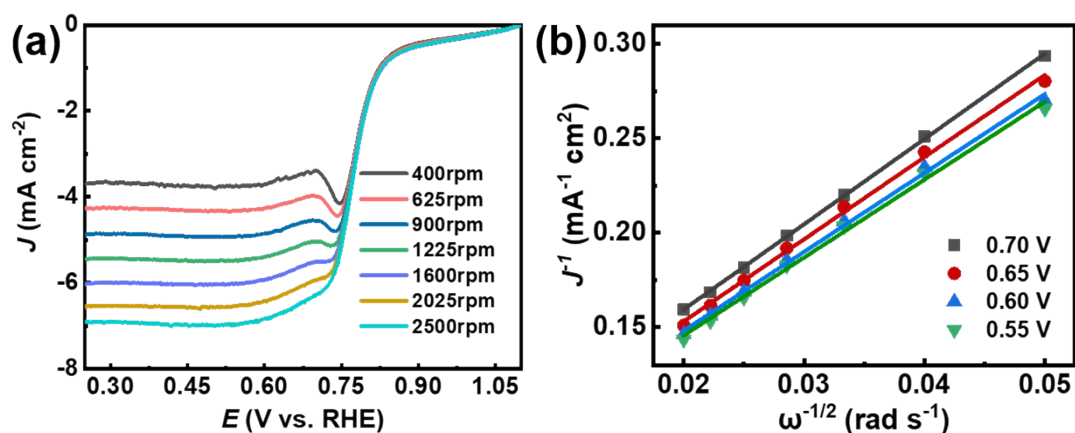


Fig. S19 (a) LSV curves at different rotating rates and (b) Koutecky-Levich (K-L) plots of the $\text{Fe}_1/d\text{-CN}$ catalyst in O_2 saturated 0.5 M H_2SO_4 solution.

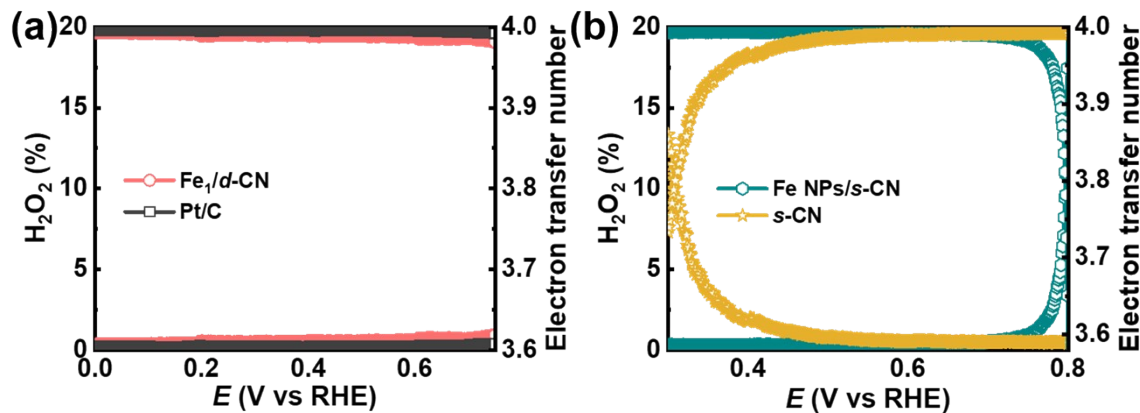


Fig. S20 Electron transfer number and peroxide yield derived from ring-disk voltammograms of the $\text{Fe}_{1/d}\text{-CN}$, Fe NPs/s-CN, s-CN and commercial Pt/C catalysts in O_2 saturated 0.5 M H_2SO_4 solution.

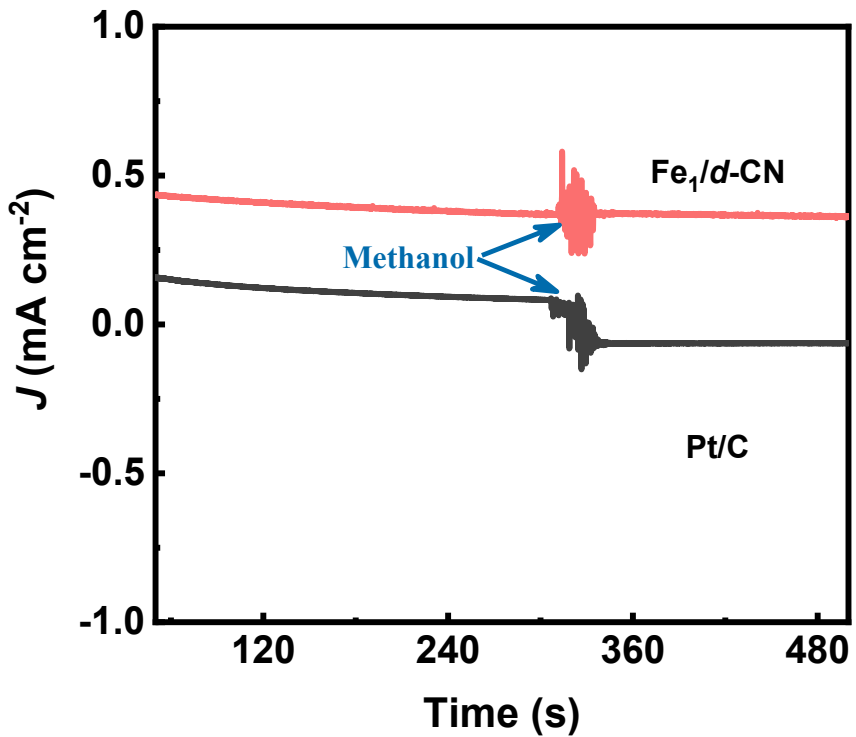


Fig. S21 Methanol tolerance of the $\text{Fe}_1/d\text{-CN}$ and commercial Pt/C catalysts in O_2 saturated 0.5 M H_2SO_4 solution.

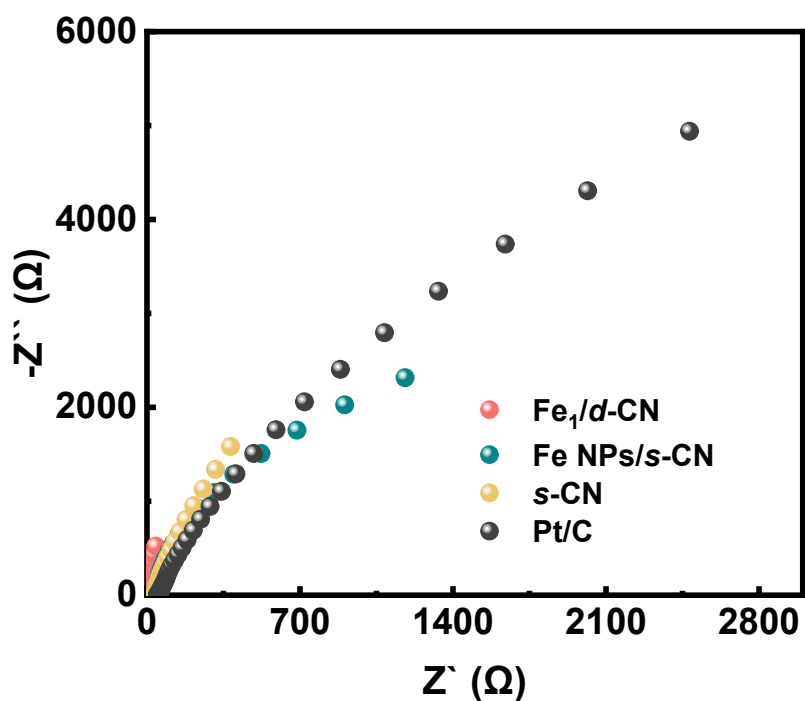


Fig. S22 Nyquist plots of $\text{Fe}_1/d\text{-CN}$ and control samples in O_2 saturated 0.5 M H_2SO_4 solution.

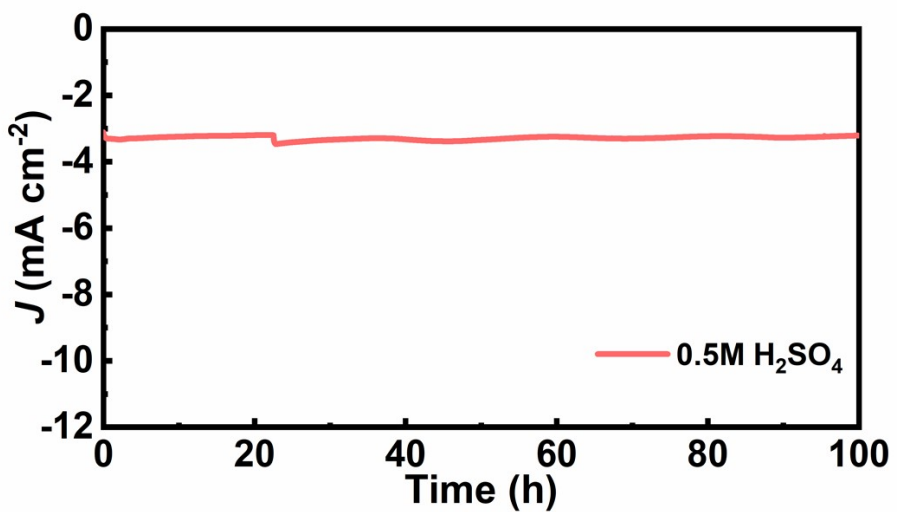


Fig. S23 I-t chronoamperometric responses of the $\text{Fe}_1/d\text{-CN}$ catalyst in the acidic media.

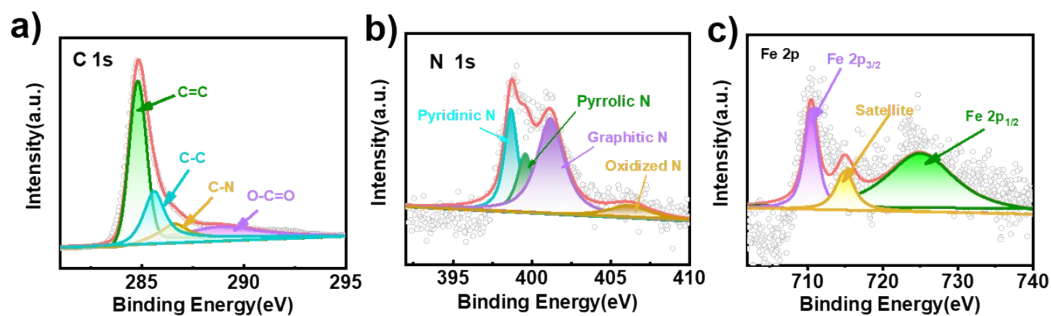


Fig. S24 High-resolution XPS spectra of (a) C 1s, (b) N 1s, and (c) Fe 2p for $\text{Fe}_1/d\text{-CN}$ catalyst after 30 k CV cycles in 0.5 M H_2SO_4 solution.

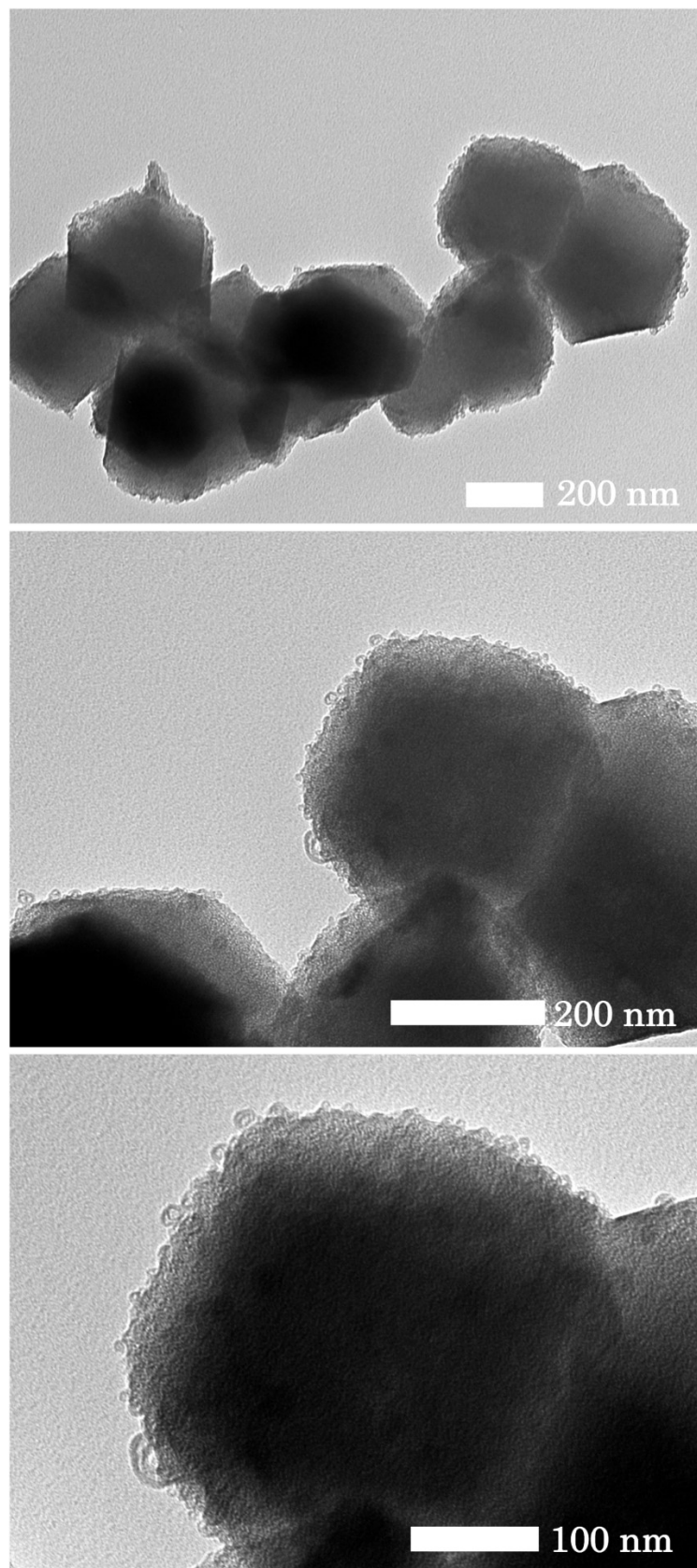


Fig. S25 TEM images of the $\text{Fe}_{1/d}\text{-CN}$ catalyst after 30 k CV cycles in 0.5 M H_2SO_4 solution.

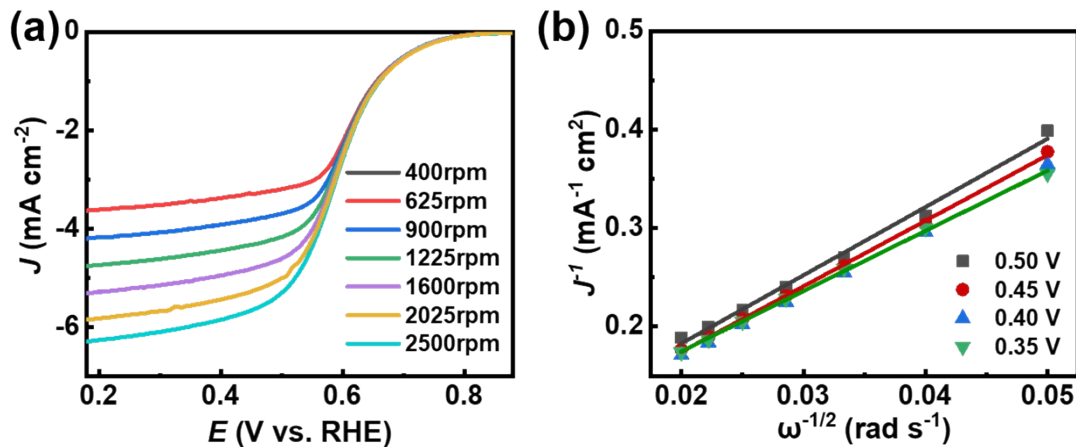


Fig. S26 (a) LSV curves at different rotating rates and (b) Koutecky-Levich (K-L) plots of the $\text{Fe}_1/d\text{-CN}$ catalyst in O_2 saturated 0.1 M phosphate buffer solution.

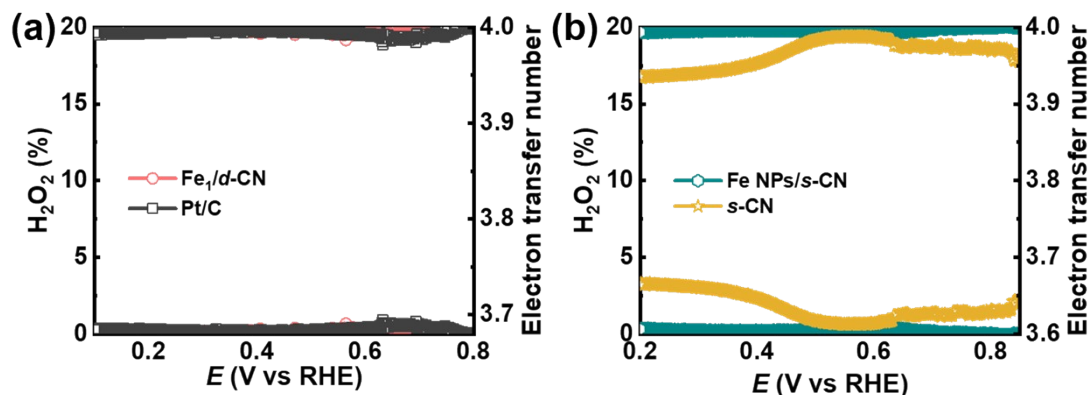


Fig. S27 Electron transfer number and peroxide yield derived from ring-disk voltammograms of the $\text{Fe}_1/d\text{-CN}$, Fe NPs/s-CN, s-CN and commercial Pt/C catalysts in O_2 saturated 0.1 M phosphate buffer solution.

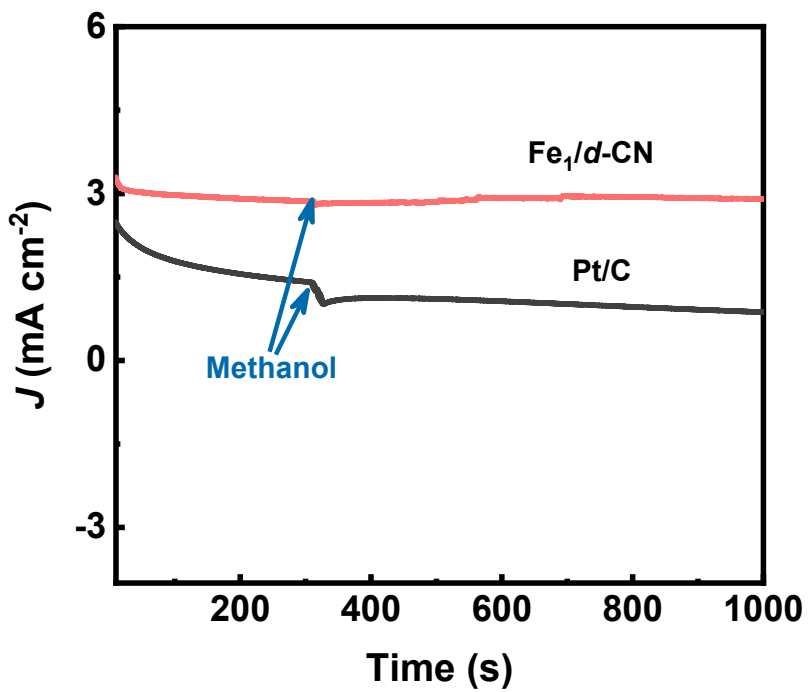


Fig. S28 Methanol tolerance of the $\text{Fe}_1/d\text{-CN}$ and commercial Pt/C catalysts in O_2 saturated 0.1 M phosphate buffer solution.

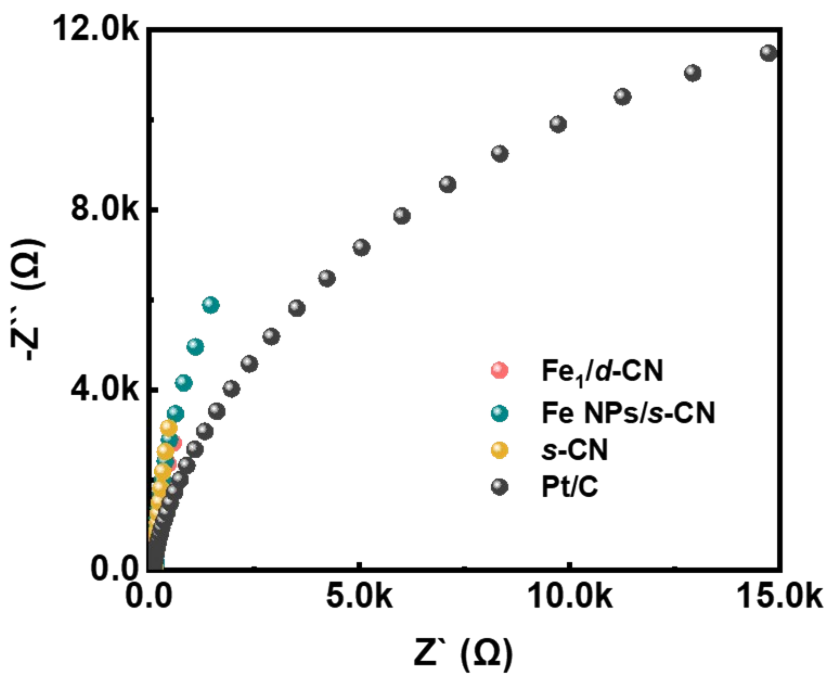


Fig. S29 Nyquist plots of the $\text{Fe}_1/d\text{-CN}$ catalyst and control samples in O_2 saturated 0.1 M phosphate buffer solution.

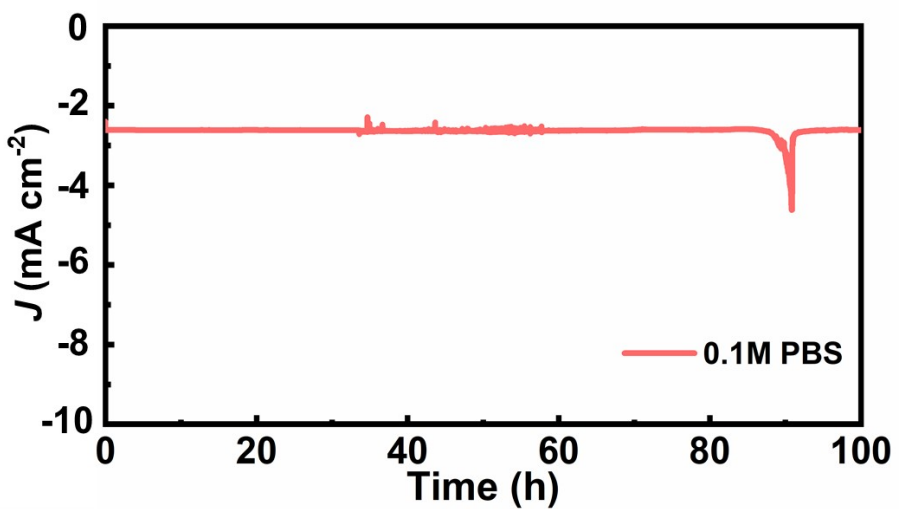


Fig. S30 I-t chronoamperometric responses of the $\text{Fe}_1/d\text{-CN}$ catalyst in the neutral media.

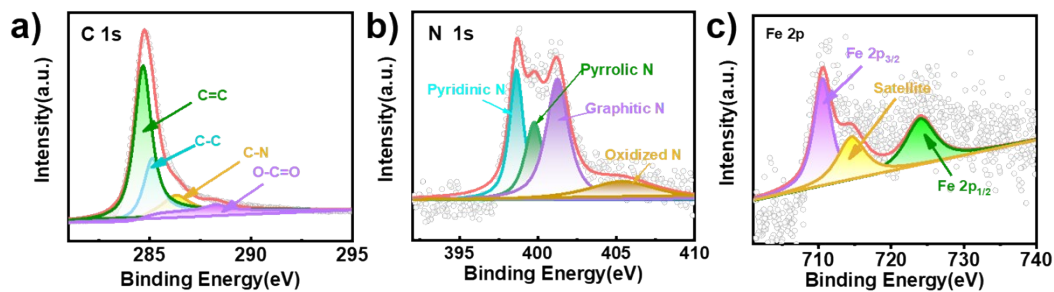


Fig. S31 High-resolution XPS spectra of (a) C 1s, (b) N 1s, and (c) Fe 2p for $\text{Fe}_1/d\text{-CN}$ catalyst after 30 k CV cycles in 0.1 M PBS solution.

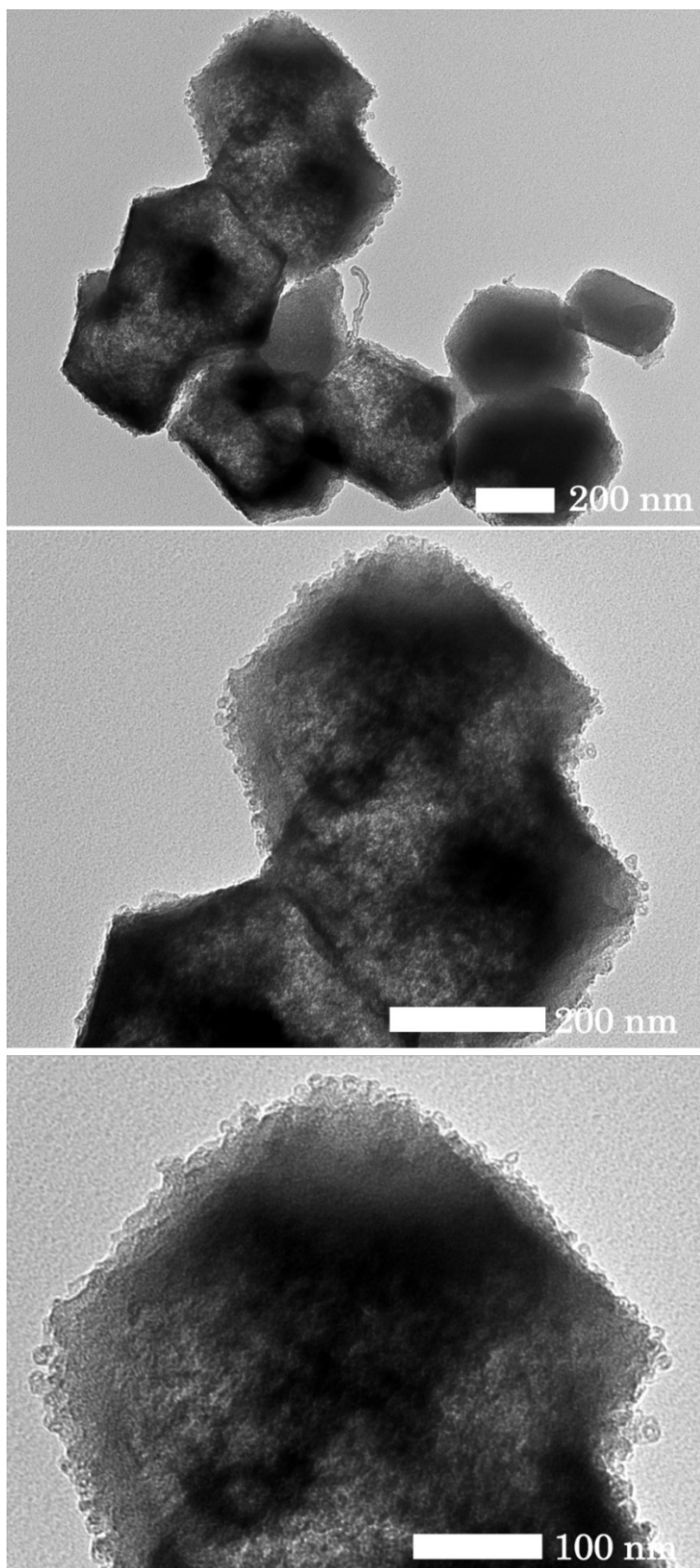


Fig. S32 (a-c) TEM images of the $\text{Fe}_1/d\text{-CN}$ catalyst after 30 k CV cycles 0.1 M phosphate buffer solution.

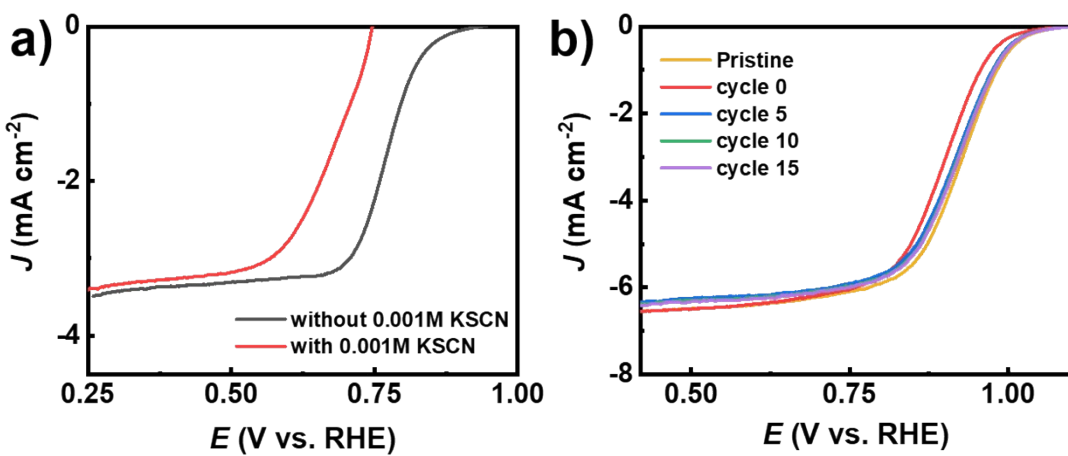


Fig. S33 a) ORR polarization curves of $\text{Fe}_1/d\text{-CN}$ catalyst in O_2 -saturated 0.1 M HClO_4 with or without 0.01 M KSCN . b) SCN^- -poisoned $\text{Fe}_1/d\text{-CN}$ in 0.1M KOH .

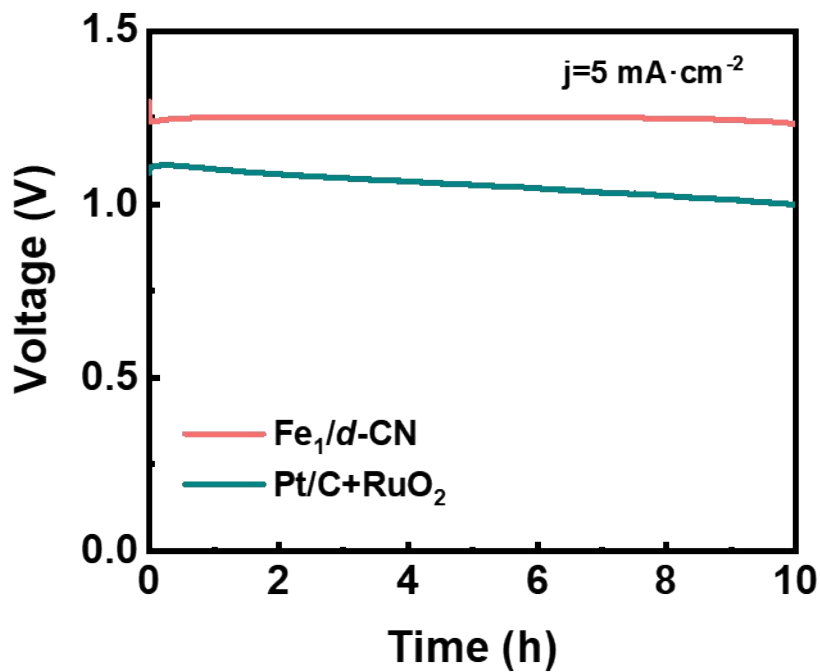


Fig. S34 Constant current discharge curves of flexible quasi-solid-state ZABs in alkaline electrolyte with air cathodes of the $\text{Fe}_1/d\text{-CN}$ and Pt/C+RuO_2 catalyst at 5 mA cm^{-2} .

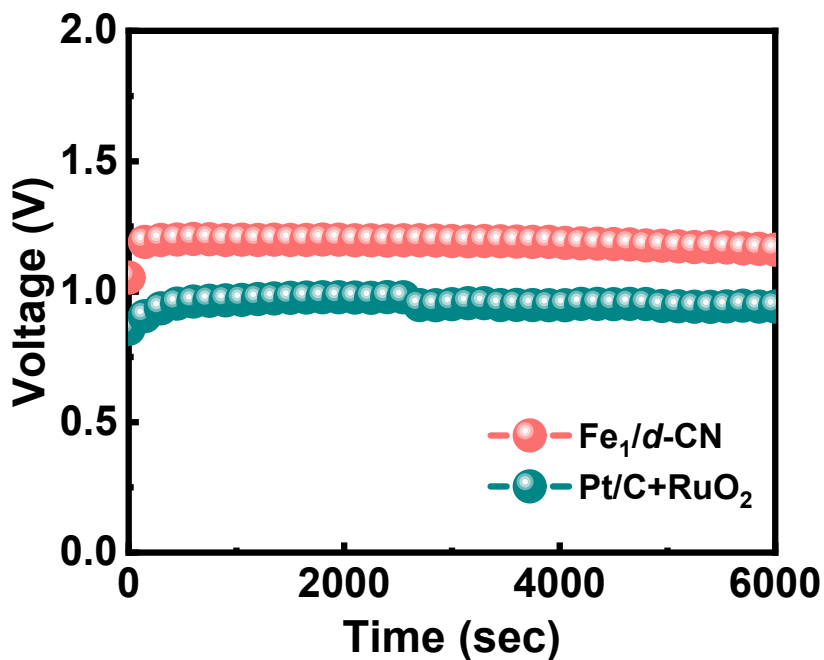


Fig. S35 Open-circuit curves of flexible quasi-solid-state ZABs in neutral electrolyte with air cathodes of the $\text{Fe}_1/d\text{-CN}$ and $\text{Pt}/\text{C}+\text{RuO}_2$ catalysts, respectively.

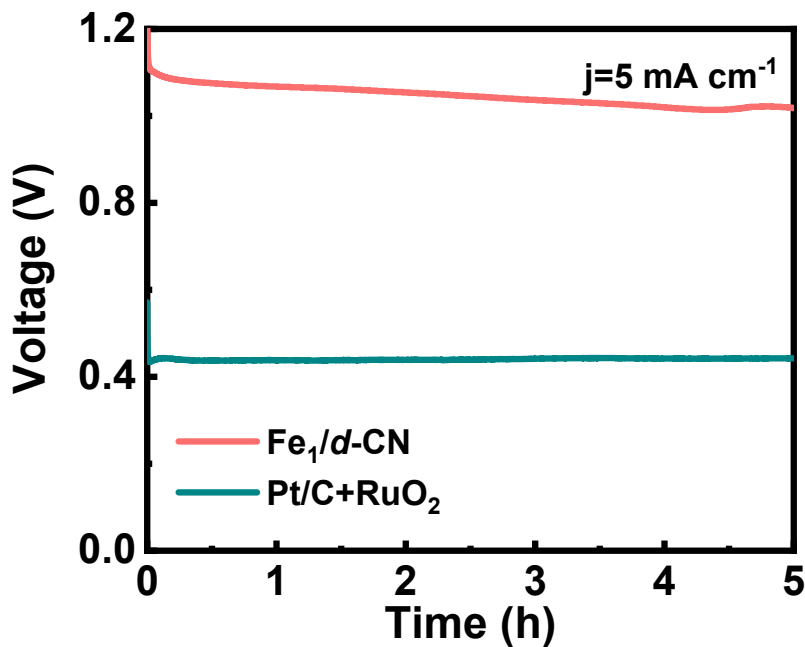


Fig. S36 Constant current discharge curves of flexible quasi-solid-state ZABs in neutral electrolyte with air cathodes of the $\text{Fe}_1/d\text{-CN}$ and $\text{Pt}/\text{C}+\text{RuO}_2$ catalyst at 5 mA cm^{-2} .

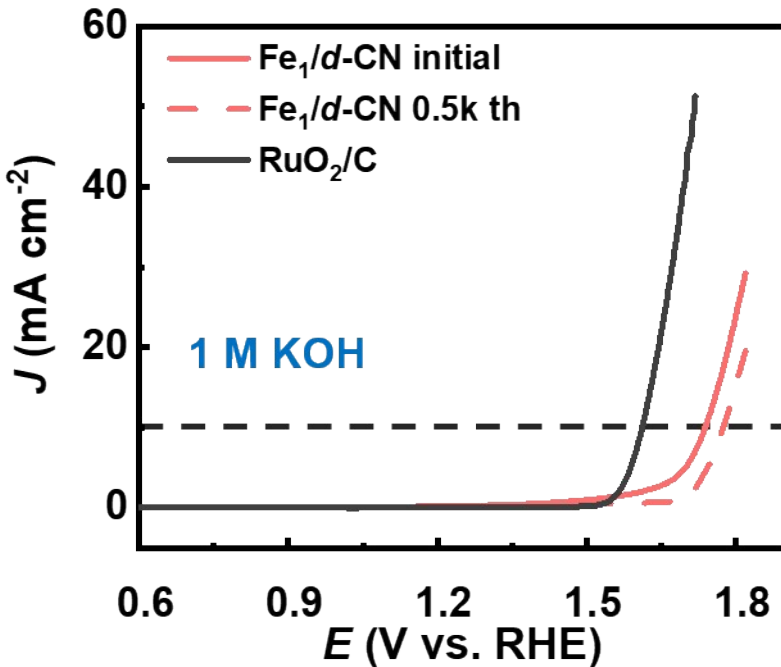


Fig. S37 LSV polarization curves of the Fe₁/d-CN catalyst before and after 0.5k cycling text, and the RuO₂/C catalyst for OER in 1 M KOH media.

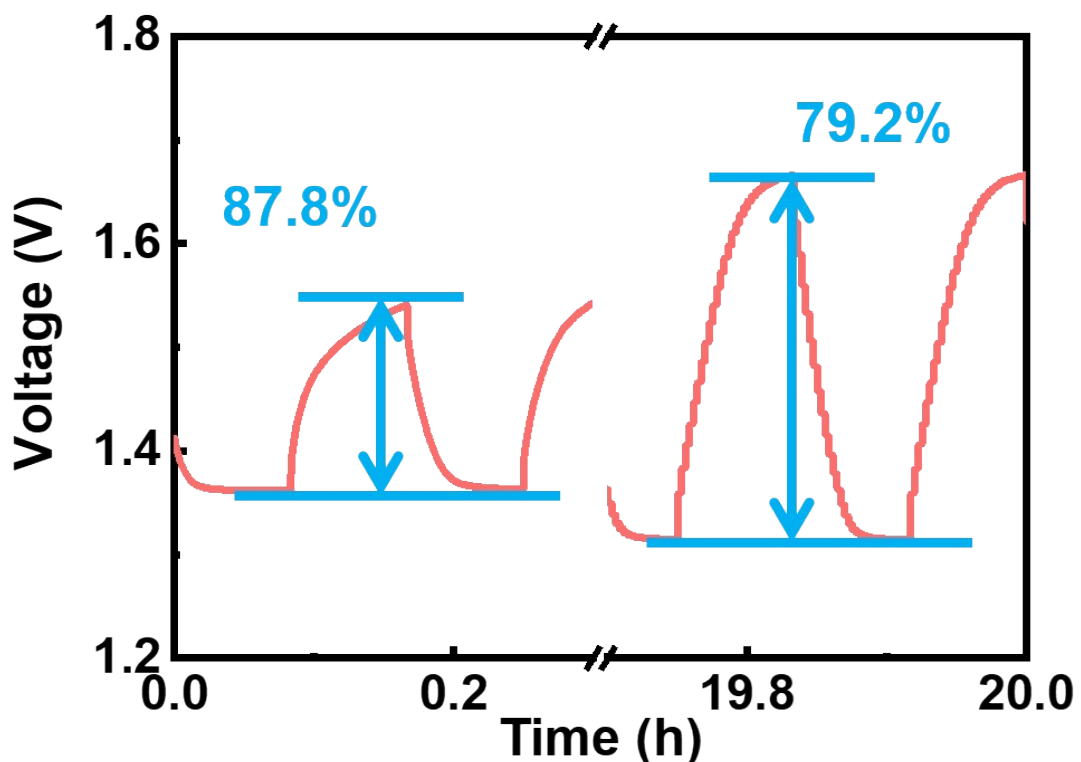


Fig. S38 The first and the last discharge-charge curves of Fe₁/d-CN-based flexible quasi-solid-state alkaline Zn-air batteries at 1 mA cm^{-2} with simply improved packaging technology.

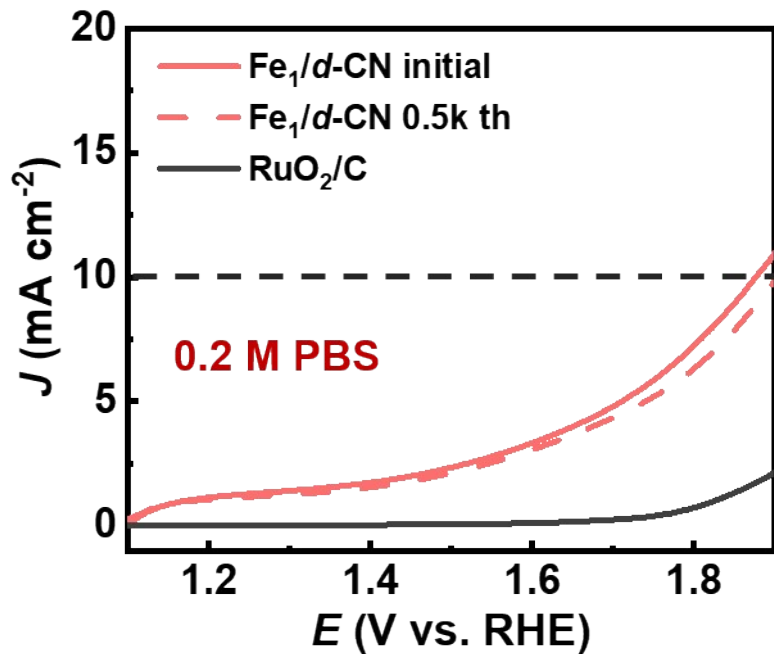


Fig. S39 LSV polarization curves of the $\text{Fe}_1/\text{d-CN}$ catalyst before and after 0.5k cycling text, and the RuO_2/C catalyst for OER in 0.2 M PBS media.

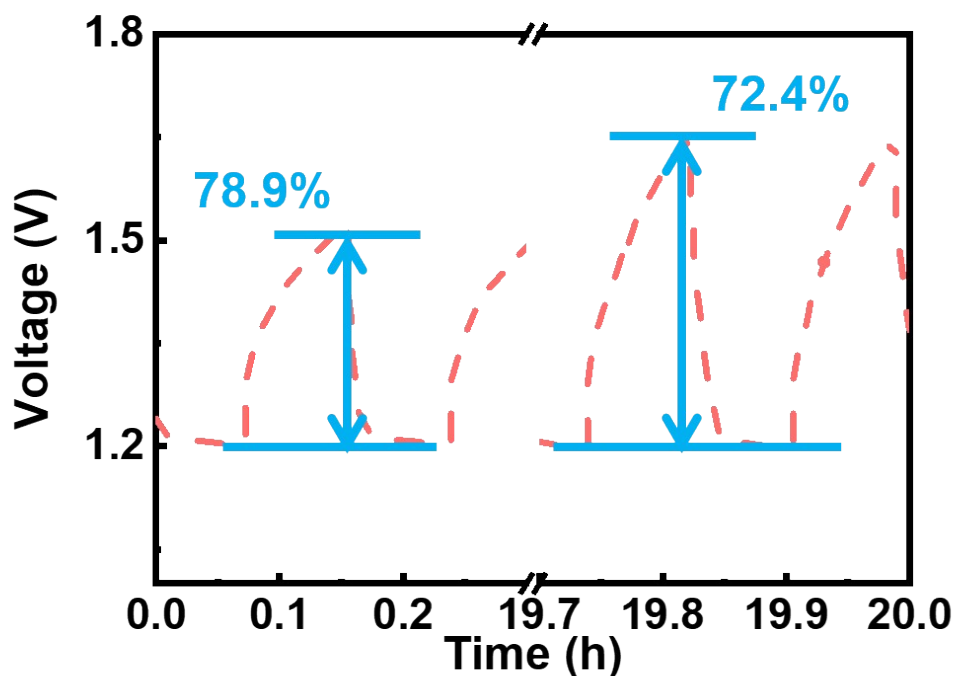


Fig. S40 The first and the last discharge-charge curves of $\text{Fe}_1/\text{d-CN}$ -based flexible quasi-solid-state neutral Zn-air batteries at 1 mA cm^{-2} with simply improved packaging technology.

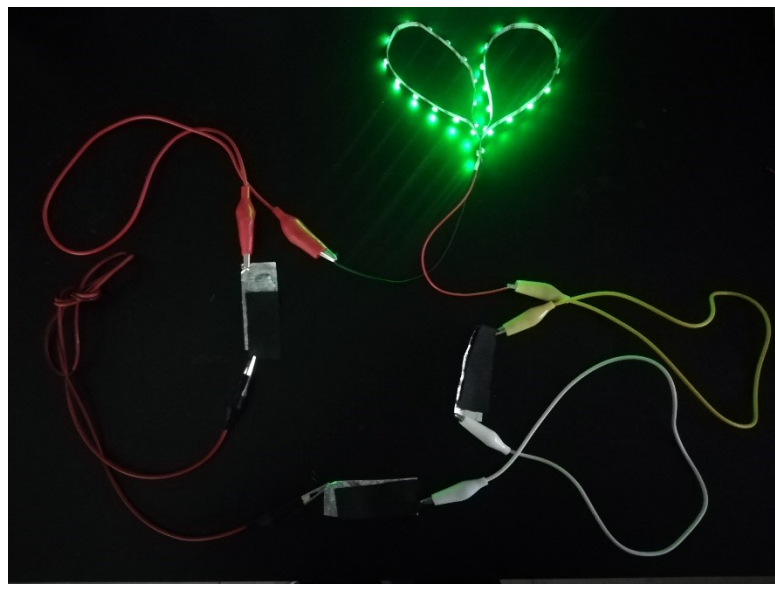


Fig. S41 A heart-shape LED strip lit by three flexible quasi-solid-state Zn-air batteries in neutral electrolyte.

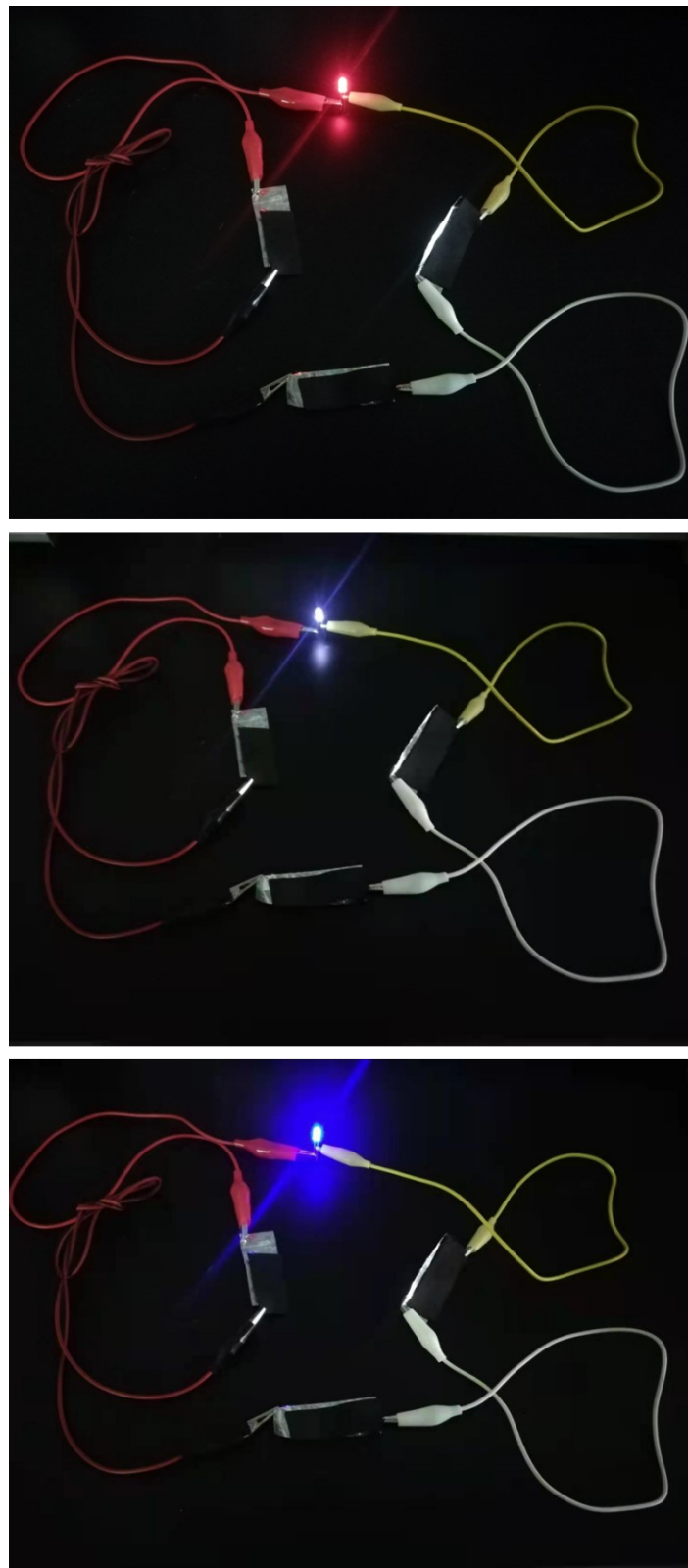


Fig. S42 A red/white/blue LED panel lit by three flexible quasi-solid-state Zn-air batteries in neutral electrolyte.

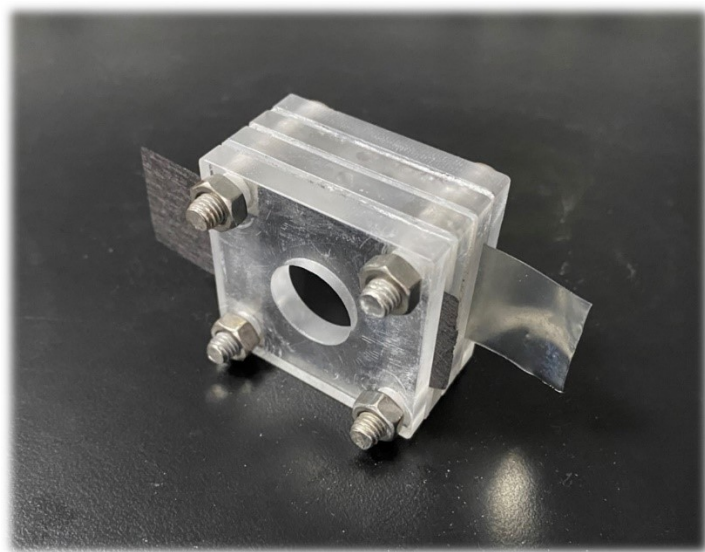


Fig. S43 Photograph of the liquid alkaline/neutral Zn–air batteries with air cathodes of the $\text{Fe}_1/d\text{-CN}$ and Pt/C+RuO_2 catalysts. (alkaline condition: 6 M KOH+0.2 M $\text{Zn}(\text{ac})_2$, neutral condition: 4 M $\text{NH}_4\text{Cl}+2\text{M KCl}$)

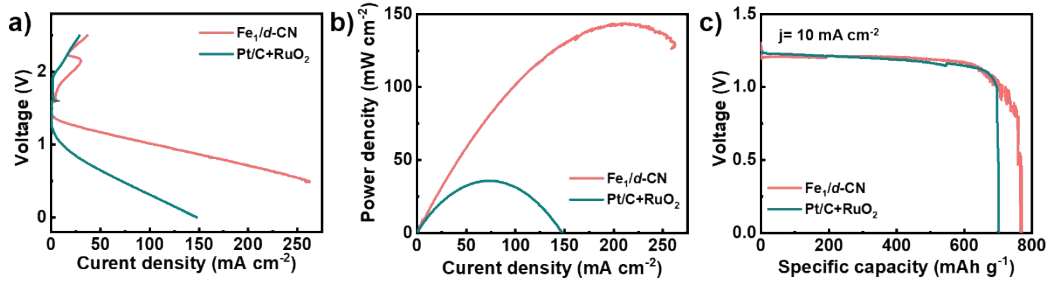


Fig. S44 (a) Charge-discharge polarization curves, (b) Power density curves, (c) Constant current discharge curves at 10 mA cm^{-2} of the liquid alkaline Zn–air batteries with air cathodes of the Fe₁/d-CN and Pt/C+RuO₂ catalysts.

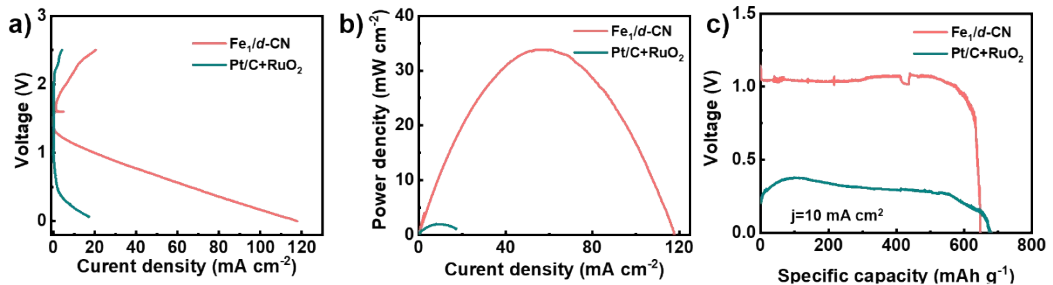


Fig. S45 (a) Charge-discharge polarization curves, (b) Power density curves, (c) Constant current discharge curves at 10 mA cm^{-2} of the liquid neutral Zn–air batteries with air cathodes of the Fe₁/d-CN and Pt/C+RuO₂ catalysts.

For the exhibited energy efficiency, the Fe₁/d-CN-based battery achieves 34.0 mW cm^{-2} at 57 mA cm^{-2} of the peak power density, outperforming the Pt/C+RuO₂-based battery (2.0 mW cm^{-2} at 9.5 mA cm^{-2}) (Fig. S31b). The specific capacity of the Fe₁/d-CN-based is 653 mA h g^{-1} at a discharging current density of 10 mA cm^{-2} corresponding to energy density of 662 W h kg^{-1} . Though the Pt/C+RuO₂-based battery delivered a specific capacity of 676 mA h g^{-1} , the lower discharging voltage led to limited energy density of 281 W h kg^{-1} (Fig. S31c, and Table S10, S11).

Table S1. The ICP-MS data of the Fe catalysts with different Fe ratios.

Sample	Element	Content(wt%)
Fe-0.002M	Fe	1.28
Fe-0.006M		1.59
Fe-0.010M		1.82
Fe_{1/d}-CN (Fe-0.014M)		2.04
Fe-0.018M		2.41
Fe-0.022M		2.89

Table S2. Structural parameters extracted from the Fe K-edge EXAFS fitting parameters. ($S_0^2 = 0.71$)

Sample	Scattering pair	CN	R(Å)	σ^2 (10 ⁻³ Å ²)	ΔE_0 (eV)	R factor
Fe _{1/d} -CN	Fe-N1	1.8	1.85	0.002	1.0	0.009
	Fe-N2	2.7	2.02	0.002		
	Fe-N3	3.5	2.48	0.002		

S_0^2 : the amplitude reduction factor ($S_0^2 = 0.71$ was obtained by Fe foil reference); CN is the coordination number; R: interatomic distance (the bond length between central atoms and surrounding coordination atoms); σ^2 : Debye-Waller factor; ΔE_0 : the inner potential. R factor: goodness of fit. Error bounds that characterize the structural parameters obtained by EXAFS spectroscopy were estimated as $N \pm 20\%$; $R \pm 1\%$; $\sigma^2 \pm 20\%$; $\Delta E_0 \pm 20\%$. (FT range: 1.8-11.0 Å⁻¹; fitting range: 1.0-3.0 Å)

Table S3. Comparison of the ORR performance of Fe₁/*d*-CN, Fe NPs/*s*-CN, *s*-CN and Pt/C in O₂-saturated 0.1 M KOH, 0.5 M H₂SO₄ and 0.1M PBS solutions at 1600 rpm.

Catalyst	<i>E</i> _{onset} (V vs. RHE)	<i>E</i> _{1/2} (V vs. RHE)	<i>E</i> _k (mA cm ⁻¹)	Tafel slop(mV dec ⁻¹)	Decay in <i>E</i> _{1/2} of stability (mV)	Electrolyte
			<i>E</i> _k @0.9V			
Fe ₁ / <i>d</i> -CN	1.05	0.950	22.68	54	1/30k cycl.	0.1 M KOH
Fe NPs/ <i>s</i> -CN	0.98	0.862	1.51	74	-	
<i>s</i> -CN	0.96	0.788	1.46	130	-	
Pt/C	0.99	0.863	0.92	64	7/2k cycl.	
			<i>E</i> _k @0.75V			
Fe ₁ / <i>d</i> -CN	0.91	0.781	25.59	64	10/30k cycl.	0.5 M H ₂ SO ₄
Fe NPs/ <i>s</i> -CN	0.79	0.610	0.49	148	-	
<i>s</i> -CN	0.72	0.517	0.74	196	-	
Pt/C	0.90	0.790	26.25	87	55/2k cycl.	
			<i>E</i> _k @0.55V			
Fe ₁ / <i>d</i> -CN	0.75	0.605	17.08	98	1/30k cycl.	0.1 M PBS
Fe NPs/ <i>s</i> -CN	0.69	0.575	9.35	96	-	
<i>s</i> -CN	0.61	0.484	3.01	100	-	
Pt/C	0.75	0.595	7.31	123	47/2k cycl.	

Table S4. Comparison of ORR performance in alkaline media of $\text{Fe}_1/d\text{-CN}$ at 1600 rpm with reported representative non-precious electrocatalysts.

Catalyst	E_{onset} (V vs. RHE)	$E_{1/2}$ (V vs. RHE)	ΔE (mV) ($E_{1/2}$ catalyst- $E_{1/2}$ Pt/C)	$E_k@0.9V$ (mA cm ⁻²)	Tafel slop (mV decade ⁻¹)	Electrolyte	Ref.
Fe₁/d-CN	1.05	0.950	87	22.7	54	0.1 M KOH	This work
Fe-N/P-C-700	0.941	0.867	36	1.86	-		2
FeSA-N-C	0.99	0.9	40	6.1	-		3
Fe@Aza-PON	0.9	0.839	13	0.545	60		4
Fe SAs-N/C-20	0.97	0.909	59	10.1	-		5
SA-Fe-HPC	0.96	0.89	50	3.72	41		6
Fe-SAs/NPS-HC	0.97	0.912	72	13	36		7
3Fe-N-C HNSs	1.045	0.87	30	-	67		8
p-Fe-N-CNFs	0.91	0.82	0	-	-		9
FeNC-S-FexC/Fe	1.05	0.873	40	5.45	-		10
FePc/Ti ₃ C ₂ T _x	0.97	0.89	20	3.0	-		11
FePx/Fe-N-C/NPC	1.01	0.86	20	-	-		12
Fe-N-C-900	0.99	0.927	67	≈11	71.8		13
1MIL/40ZIF-1000	≈1.0	0.88	60	-	-		14

Table S5. Comparison of ORR performance in acidic media of Fe₁/*d*-CN at 1600 rpm with reported representative non-precious electrocatalysts.

Catalyst	<i>E</i> _{onset} (V vs. RHE)	<i>E</i> _{1/2} (V vs. RHE)	<i>ΔE</i> (mV) (<i>E</i> _{1/2} catalyst- <i>E</i> _{1/2} Pt/C)	<i>E</i> _{k@0.75V} (mA cm ⁻¹)	Tafel slop (mV decade ⁻¹)	Electrolyte	Ref.
Fe ₁ / <i>d</i> -CN	0.91	0.781	-9	25.6	64	0.5 M H ₂ SO ₄	This work
1MIL/40ZIF-1000	0.93	0.79	-6	-	52		14
HCS-A	≈0.87	0.75	≈-2	-	63		15
Fe/N/S-CNT	0.80	0.62	-14	-	-		16
Fe-N-SCNN	0.89	0.78	-15	-	-		17
Cu@Fe-N-C	0.88	0.76	-43	-	81		18
Fe-N-C	0.92	0.78	-12	14.8	54.2		19
Fe, N-HPCC	0.90	0.76	-50	-	61		20
Fe SA-N-C	0.93	0.78	-5	9.6	-		21
C-FeZIF-1.44-950	0.91	0.78	-60	-	-		22

Table S6. Comparison of ORR performance in neutral media of Fe₁/*d*-CN at 1600 rpm with reported representative non-precious electrocatalysts.

Catalyst	E_{onset} (V vs. RHE)	$E_{1/2}$ (V vs. RHE)	$\Delta E(\text{mV})$ ($E_{1/2}$ catalyst- $E_{1/2}$ Pt/C)	Electrolyte	Ref.
Fe ₁ / <i>d</i> -CN	0.75	0.605	10	0.1 M PBS	This work
Fe-N-C/800-HT2	0.862	0.743	-47		23
Fe ₃ O ₄ @N/Co-C	0.72	0.53	-60		24
Fe,N/PGC-30	0.85	0.61	0		25
Fe@BC-800	0.86	0.68	-30		26
Cu-CTF/CP	0.81	0.59	-190		27

Table S7. Comparison of $E_{1/2}$ in alkaline, acidic and neutral media of $\text{Fe}_1/d\text{-CN}$ and the previously reported PH-universal ORR catalysts.

Catalyst	Alkaline		Acidic		Neutral		Ref.
	$E_{1/2}$ (V vs. RHE)	ΔE (mV) ($E_{1/2}$ catalyst- $E_{1/2}$ Pt/C)	$E_{1/2}$ (V vs. RHE)	ΔE (mV) ($E_{1/2}$ catalyst- $E_{1/2}^-$ Pt/C)	$E_{1/2}$ (V vs. RHE)	ΔE (mV) ($E_{1/2}$ catalyst- $E_{1/2}^-$ Pt/C)	
$\text{Fe}_1/d\text{-CN}$	0.95	87	0.78	-9	0.60	10	This work
Fe/NC-3	0.9	10	0.71	-92	0.687	-49	28
NPF-CNS-2	0.81	≈40	0.7	≈-80	0.58	≈-70	29
MCHS-9:1	≈0.75		≈0.21		≈0.5		30
FeS/Fe ₃ C@N-S-C-800	0.87	30	0.64	-160	0.54	-15	31
B-FeOOH/PNGNs	0.88	41	0.68	-70	0.69	17	32
g-N-CNPs	0.694		0.366		0.354		33
FeCo SAs@Co/N-GC	0.88	40	0.84(0.1 M HClO 4)		0.84		40

Table S8. Comparison of the alkaline/neutral flexible quasi-solid-state Zn-air batteries with the Fe₁/*d*-CN, and Pt/C+ RuO₂ catalysts as the air-cathode catalysts.

	Electrolyte		Fe ₁ / <i>d</i> -CN	Pt/C+RuO ₂
Flexible quasi-solid-state Zn-air batteries	KOH- PVA	Open voltage (V)	1.50	1.22
		Peak power density (mW cm ⁻²)	78	22
		Ddischarge voltage (V)	1.25	1.05
	NH ₄ Cl+ZnCl ₂ -PVA	Open voltage (V)	1.21	0.95
		Peak power density (mW cm ⁻²)	15.8	3.4
		Ddischarge voltage (V)	1.05	0.44

Table S9. Summary of performance based on non-precious metal catalysts for quasi-solid-state Zn-air batteries with alkaline electrolyte.

Materials	Electrolyte	Open voltage (V)	Peak power density (mW cm ⁻²)	Rfe.
Fe₁/d-CN	KOH-PVA	1.50	78	This work
NPC/FeCo@NCNT	KOH-PVA	1.45	65	34
NiFe/NCNF/CC	KOH-PAM	-	76.6	35
Co/N@CNTs@CNM-800	KOH-PAM	1.4	26.5	36
Co-SAs@NC	KOH-PAM	1.4	-	37
IOSHs-NSC	KOH-PAM-co-PAA	1.408	60	38
CoN ₄ /NG	KOH-PVA	-	~28	39

Table S10. Comparison of the alkaline/neutral liquid Zn-air batteries with the $\text{Fe}_{1/d}\text{-CN}$, and Pt/C+RuO_2 catalysts as the air-cathode catalysts.

	Electrolyte		$\text{Fe}_{1/d}\text{-CN}$	Pt/C+RuO_2
liquid Zn-air batteries	6 M KOH +0.2 M $\text{Zn}(\text{ac})_2$	Peak power density (mW cm^{-2})	144	36
		Specific capacity (mA h g Zn^{-1})	770	702
		Energy density (Wh kg Zn^{-1})	890	828
	4 M NH_4Cl +2M KCl	Peak power density (mW cm^{-2})	34	2
		Specific capacity (mA h g Zn^{-1})	653	676
		Energy density (Wh kg Zn^{-1})	662	281

Table S11. Summary of performance based on non-precious metal catalysts for liquid Zn-air batteries with alkaline/neutral electrolyte.

Materials	Liquid Zn-air batteries				
	Electrolyte	Peak power density (mW cm ⁻²)	Specific capacity@10 mA cm ⁻² (mA h g Zn ⁻¹)	Energy density (Wh kg Zn ⁻¹)	Rfe.
Fe_{1/d}-CN	6 M KOH +0.2 M Zn(Ac) ₂	144	770	890	This work
NiFe/NCNF/CC		140.1	730	-	35
IOSHs-NSC-Co ₉ S ₈		133	768	937	38
Co@NCNTs-800		123.4	698	837	41
Co/N@CNTs@CNM-800		103	403	505	43
C-MOF-C ₂ -900	6 M KOH +2 M Zn(OAc) ₂	105	741	-	42
Fe_{1/d}-CN	4 M NH ₄ Cl+2M KCl	34	653	662	This work
PMO/N-rGO	2 M NH ₄ Cl+0.2 M ZnCl ₂ +0.02 M MnSO ₄	7.3	488.3	420	44
MnO/CNT	ZnCl ₂ –NH ₄ Cl–NH ₄ OH	-	58	67	45

MnOx	0.1M NH ₄ Cl pH 7	13.8	-	-	46
Fe-Co/C-N	0.5M KNO ₃	32	-	-	47

References

- 1 Y. J. Chen, S. F. Ji, Y. G. Wang, J. C. Dong, W. X. Chen, Z. Li, R. A. Shen, L. R. Zheng, Z. B. Zhuang, D. S. Wang, and Y. D. Li, *Angew. Chem. Int. Ed.*, 2017, **56**, 1-6.
- 2 K. Yuan, D. Lützenkirchen-Hecht, L. B. Li, L. Shuai, Y. Z. Li, R. Cao, M. Qiu, X. D. Zhuang, M. K. H. Leung, Y. W. Chen, U. Scherf, *J. Am. Chem. Soc.*, 2020, **142**, 2404-2412.
- 3 L. Jiao, R. Zhang, G. Wan, W. Yang, X. Wan, H. Zhou, J. Shui, S. H. Yu, H. L. Jiang, *Nat. Commun.*, 2020, **11**, 2831.
- 4 S. J. Kim, J. Mahmood, C. Kim, G. F. Han, S. W. Kim, S. M. Jung, G. Zhu, J. J. De Yoreo, G. Kim, J. B. Baek, *J. Am. Chem. Soc.*, 2018, **140**, 1737-1742.
- 5 R. Jiang, L. Li, T. Sheng, G. Hu, Y. Chen, L. Wang, *J. Am. Chem. Soc.*, 2018, **140**, 11594-11598.
- 6 Z. Zhang, J. Sun, F. Wang, L. M. Dai, *Angew. Chem. Int. Ed.*, 2018, **57**, 9038-9043.
- 7 Y. Chen, S. Ji, S. Zhao, W. Chen, J. Dong, W. C. Cheong, R. Shen, X. Wen, L. Zheng, A. I. Rykov, S. Cai, H. Tang, Z. Zhuang, C. Chen, Q. Peng, D. Wang, Y. Li, *Nat. Commun.*, 2018, **9**, 5422.
- 8 Y. Chen, Z. Li, Y. Zhu, D. Sun, X. Liu, L. Xu, Y. Tang, *Adv. Mater.*, 2019, **31**, 1806312.
- 9 B. C. Hu, Z. Y. Wu, S. Q. Chu, H. W. Zhu, H. W. Liang, J. Zhang, S. H. Yu, *Energy Environ. Sci.*, 2018, **11**, 2208-2215.
- 10 Y. Qiao, P. Yuan, Y. Hu, J. Zhang, S. Mu, J. Zhou, H. Li, H. Xia, J. He, Q. Xu, *Adv. Mater.*, 2018, **30**, 1804504.
- 11 Z. Li, Z. Zhuang, F. Lv, H. Zhu, L. Zhou, M. Luo, J. Zhu, Z. Lang, S. Feng, W. Chen, L. Mai, S. Guo, *Adv. Mater.*, 2018, **30**, 1803220.
- 12 Q. Qin, H. Jang, P. Li, B. Yuan, X. Liu, J. Cho, *Adv. Energy Mater.*, 2019, **9**, 1803312.
- 13 C. Zhu, Q. Shi, B. Z. Xu, S. Fu, G. Wan, C. Yang, S. Yao, J. Song, H. Zhou, D. Du, S. P. Beckman, D. Su, Y. Lin, *Adv. Energy Mater.*, 2018, **8**, 1801956.
- 14 H. Wang, F. X. Yin, N. Liu, R. H. Kou, X. B. He, C. Sun, B. H. Chen, D. J. Liu, H.

- Q. Yin, *Adv. Funct. Mater.*, 2019, **29**, 1901531.
- 15 P. Xu, J. Zhang, G. Jiang, F. Hassan, J. Y. Choi, X. Fu, P. Zamani, L. Yang, D. Banham, S. Ye, Z. Chen, *Nano Energy.*, 2018, **51**, 745-753.
- 16 Z. Tan, H. Li, Q. Feng, L. Jiang, H. Pan, Z. Huang, Q. Zhou, H. Zhou, S. Ma, Y. Kuang, *J. Mater. Chem. A.*, 2019, **7**, 1607-1615.
- 17 H. Jina, H. Zhoua, D. Hea, Z. Wanga, Q. Wua, Q. Lianga, S. Liuc, S. Mu, *Appl. Catal. B: Envir.*, 2019, **250**, 143-149.
- 18 Z. Wang, H. Jin, T. Meng, K. Liao, W. Meng, J. Yang, D. He, Y. Xiong, S. Mu, *Adv. Funct. Mater.*, 2018, **28**, 1802596.
- 19 M. Xiao, J. Zhu, L. Ma, Z. Jin, J. Ge, X. Deng, Y. Hou, Q. He, J. Li, Q. Jia, S. Mukerjee, R. Yang, Z. Jiang, D. Su, C. Liu, W. Xing, *ACS Catal.*, 2018, **8**, 2824-2832.
- 20 Z. Guo, Z. Zhang, Z. Lia, M. Dou, F. Wang, *Nano Energy.*, 2019, **57**, 108-117.
- 21 L. Jiao, G. Wan, R. Zhang, H. Zhou, S. H. Yu, H. L. Jiang, *Angew. Chem. Int. Ed.*, 2018, **57**, 8525-8529.
- 22 Y. Deng, B. Chi, J. Li, G. Wang, L. Zheng, X. Shi, Z. Cui, L. Du, S. Liao, K. Zang, J. Luo, Y. Hu, X. Sun, *Adv. Energy Mater.*, 2019, **9**, 1802856.
- 23 G. Zhang, L. Li, M. Chen, F. Yang, *J. Mater. Chem. A*, 2020, **8**, 9256-9267.
- 24 C. Cao, L. Wei, M. Su, G. Wang, J. Shen, *J Mater Chem A.*, 2016, **4**, 9303-9043.
- 25 W. Gu, L. Hu, J. Li, E. Wang, *J Mater Chem A.*, 2016, **4**, 14364-14370.
- 26 X. Ma, Z. Lei, W. Feng, Y. Ye, C. Feng, *Carbon.*, 2017, **123**, 481-491.
- 27 K. Iwase, T. Yoshioka, S. Nakanishi, K. Hashimoto, K. Kamiya, *Angew. Chem. Int. Ed.*, 2015, **54**, 11068-11072.
- 28 M. Liu, J. Lee, T. C. Yang, F. Zheng, J. Zhao, C. M. Yang, L. Y. S. Lee, *Small Methods*, 2021, 2001165.
- 29 Y. Zheng, H. Song, S. Chen, X. Yu, J. Zhu, J. Xu, K. A. I. Zhang, C. Zhang, T. Liu, *Small*, 2020, **16**, 2004342.
- 30 Y. Pang, K. Wang, H. Xie, Y. Sun, M. M. Titirici, G. L. Chai, *ACS Catal.*, 2020, **10**, 7434-7442.
- 31 F. Kong, X. Fan, A. Kong, Z. Zhou, X. Zhang, Y. Shan, *Adv. Funct. Mater.*, 2018,

- 28**, 1803973.
- 32 Y. Li, J. Huang, X. Hu, L. Bi, P. Cai, J. Jia, G. Chai, S. Wei, L. Dai, Z. Wen, *Adv. Funct. Mater.*, 2018, **28**, 1803330.
- 33 D. Iglesias, A. Giuliani, M. Melchionna, S. Marchesan, A. Criado, L. Nasi, M. Bevilacqua, C. Tavagnacco, F. Vizza, M. Prato, P. Fornasiero, *Chem*, 2018, **4**, 106-123.
- 34 X. Hao, Z. Jiang, B. Zhang, X. Tian, C. Song, L. Wang, T. Maiyalagan, X. Hao, Z. J. Jiang, *Adv. Sci.*, 2021, 2004572.
- 35 C. Lai, J. Fang, X. Liu, M. Gong, T. Zhao, T. Shen, K. Wang, K. Jiang, D. Wang, *Appl. Catal. B: Envir.*, 2021, **285**, 119856.
- 36 T. Liu, J. Mou, Z. Wu, C. Lv, J. Huang, M. Liu, *Adv. Funct. Mater.*, 2020, **30**, 2003407.
- 37 X. Han, X. Ling, Y. Wang, T. Ma, C. Zhong, W. Hu, Y. D. Deng, *Angew. Chem. Int. Ed.*, 2019, **58**, 5359-5364.
- 38 K. Tanga, C. Yuan, Y. Xiong, H. Hu, M. Wu, *Appl. Catal. B: Envir.*, 2020, **260**, 118209.
- 39 L. Yang, L. Shi, D. Wang, Y. Lv, D. Cao, *Nano Energy*, 2018, **50**, 691-698.
- 40 N. K. Wagh, D. H. Kim, S. H. Kim, S. S. Shinde, J. H. Lee, *ACS Nano*, 2021, doi: 10.1021/acsnano.1c04471.
- 41 Q. Wang, K. Ye, L. Xu, W. Hu, Y. Lei, Y. Zhang, Y. Chen, K. Zhou, J. Jiang, J. M. Basset, D. Wang, Y. Li, *Chem Commun*, 2019, **55**, 14801-14804.
- 42 M. Zhang, Q. Dai, H. Zheng, M. Chen, L. Dai, *Adv. Mater.*, 2018, **30**, 1705431.
- 43 X.R. Wang, J.Y. Liu, Z.W. Liu, W.C. Wang, J. Luo, X.P. Han, X.W. Du, S.Z. Qiao, J. Yang, *Adv. Mater.*, 2018, **30**, 1800005.
- 44 T. Zhang, S. Zhang, S. Cao, Q. Yao, J. Lee, *Energy Storage Mater.*, 2020, **33**, 181-187.
- 45 S. Clark, A. Mainar, E. Iruin, L. Colmenares, J. Bl'azquez, J. Tolchard, A. Latz, B. Horstmann, *J. Mater. Chem. A*, 2019, **7**, 11387-11399.
- 46 A. Sumboja, X. Ge, G. Zheng, F. Goh, T. Hor, Y. Zong, Z. Liu, *J. Power Sources*, 2016, **332**, 330-336.
- 47 L. Yu, Q. Yi, G. Li, Y. Chen, X. Yang, *J. Electrochem. Soc.*, 2018, **165**, A2502-A2509.